

The impact of Radial and Non-Radial IMF on the Earth's Magnetopause Size and Shape, and Dawn-Dusk Asymmetry from Global 3D Kinetic Simulations

Suleiman Baraka¹, Olivier Le Contel Le Contel², Lotfi Ben-Jaffel³, and Bill Moore¹

¹National Institute of Aerospace

²CNRS/Ecole Polytechnique/Sorbonne Université/Université Paris-Saclay/Obser. de Paris

³Institut d'Astrophysique de Plasma

November 30, 2022

Abstract

The boundary between the solar wind (SW) and the Earth's magnetosphere, the magnetopause (MP), is highly dynamic. Its location and shape depend on SW dynamic pressure and interplanetary magnetic field (IMF) orientation. We use a 3D kinetic Particle-In-Cell code (IAPIC) to simulate an event observed by THEMIS spacecraft on July 16, 2007. We investigate the impact of radial ($\theta_{Bx}=0^\circ$) and non-radial ($\theta_{Bx}=50^\circ$) IMF on the shape and size of Earth's MP for a dipole tilt of 31° using maximum density gradient and pressure balance methods. Using the Shue model as a reference (MP at 10.3 RE), we find that for non-radial IMF the MP expands by 1.4 and 1.7RE along the Sun-Earth (OX) and tilted magnetic equatorial (Tilt) axes, respectively, and it expands by 0.5 and 1.6RE for radial IMF along the same respective axes. When the effect of backstreaming ions is removed from the bulk flow, the expansion ranges are 1.0 and 1.3RE and 0.2, and 1.2RE, respectively. It is found that the percentage of backstreaming to bulk flow ions are 16.5% and 20% for radial and non-radial IMF. We also show that when the backstreaming ions are not identified, up to 40% of the observed expansion that is due to backstreaming particles can be inadvertently attributed to a change in the SW upstream properties. Finally, we quantified the temperature anisotropy in the magnetosheath, and observe a strong dawn-dusk asymmetry in the MP location, being more extended on the duskside than on the dawnside.

Abstract

The boundary between the solar wind (SW) and the Earth's magnetosphere, the magnetopause (MP), is highly dynamic. Its location and shape depend on SW dynamic pressure and interplanetary magnetic field (IMF) orientation. We use a 3D kinetic Particle-In-Cell code (IAPIC) to simulate an event observed by THEMIS spacecraft on July 16, 2007. We investigate the impact of radial ($\theta_{Bx}=0^\circ$) and non-radial ($\theta_{Bx}=50^\circ$) IMF on the shape and size of Earth's MP for a dipole tilt of 31° using maximum density gradient and pressure balance methods. Using the Shue model as a reference (MP at $10.3 R_E$), we find that for quasi-radial IMF the MP expands by 1.4 and $1.7R_E$ along the sun-Earth (OX) and tilted magnetic (Tilt) axes, respectively, and it expands by 0.5 and $1.6R_E$ for radial IMF along the same respective axes. When the effect of backstreaming ions is removed from the bulk flow, the expansion ranges are 1.0 and $1.3R_E$ and 0.2 , an $1.2R_E$ respectively. It is found that the percentage of backstreaming to bulk flow ions are 16.5% , and 20% for radial and non-radial IMF. We also show that when the backstreaming ions are not resolved, up to 40% of the observed expansion that is due to backstreaming particles can be inadvertently attributed to a change in the SW upstream properties. Finally, we quantified the temperature anisotropy in the magnetosheath, and observe a strong dawn-dusk asymmetry in the MP location.

Plain Language Summary

The Earth's magnetopause (MP) is a sensitive region where the pressure of the Earth magnetic field balances the shocked solar wind ram and thermal pressures. Accurate space weather monitoring and forecast require an in-depth knowledge of this region and of the physical processes that affect it. We investigate effects of the orientation of the interplanetary magnetic field (IMF) on the MP size, location, and shape by using a numerical technique (3D kinetic simulation) that explicitly resolves ion and electron motion. We are able to extract the shape and location of the MP in three dimensions to estimate the sensitivity of the MP position to the ambient IMF and solar wind conditions, while our explicit tracking of ion motions allows us to investigate the role of ion species backscattered by the

45 Earth's bow shock and magnetosheath. We find that when the IMF has a strong component
46 in the Earth-Sun direction (radial or quasi-radial IMF), these backscattered ions play an
47 important role in reducing the effective pressure of the incoming solar wind and allowing
48 the MP to expand outward.

1 Introduction

The magnetic fields of planets such as Mercury, Earth, and the giant planets present an obstacle to the supersonic solar wind (SW). As a result, a shock forms and the solar wind is redirected around the obstacle producing a cavity which is called the magnetosphere (e.g., Parks, 1991). The boundary between the solar wind and the plasma in the magnetosphere is the magnetopause (MP). At the subsolar point, the classical fluid description of the solar wind stagnation flow derives the location of the magnetopause by the balance between the planetary magnetic field pressure and the dynamic pressure of the SW. Plasma boundary layers form on either side of the magnetopause with the magnetosheath boundary layer (MSBL) on the sunward side and the low-latitude boundary layer (LLBL) on the magnetosphere side. Both layers play an important role in plasma exchange across the magnetopause (e.g., Pi et al., 2018).

The magnetopause structure is significantly influenced by the interplanetary magnetic field (IMF) orientation. While the impact of southward (Yu & Ridley, 2009; Heikkila, 2011; Tan et al., 2011; Suvorova & Dmitriev, 2015; Berchem et al., 2016) and northward IMF (Sorathia et al., 2019; Luo et al., 2013; Bobra et al., 2004; Wang et al., 2018) on the dynamics of Earth's magnetosphere have been extensively studied in the last four decades, only recently has attention been focused on radially-dominant IMF conditions, which will be called radial IMF for the remainder of this paper. For most solar wind plasma conditions at the orbital position of planets, bow shocks are collisionless and supercritical shocks, which by definition, reflect and accelerate a fraction of the plasma impinging on them. These backstreaming particles lead to the formation of the ion foreshock region upstream (e.g., Turner et al., 2018, p. 206).

Following early satellite observations (Greenstadt et al., 1968; Asbridge et al., 1968), the idea of an extended foreshock that diverts the solar wind around the magnetosphere and reduces the solar wind dynamic pressure at the subsolar magnetopause was proposed for radial IMF conditions (Fairfield et al., 1990; Merka et al., 2003; Jelínek et al., 2010;

76 Suvorova et al., 2010). The distance and shape of the equatorial magnetopause is strongly
77 affected by radial IMF, resulting in a global expansion of the magnetopause (Grygorov et al.,
78 2017). (Zhang et al., 2019) found that a dawn-dusk asymmetry exists in the magnetosheath,
79 directly related to the IMF orientation. Evidently, the plasma distribution and the IMF are
80 correlated to these asymmetries which are either generated at the bow shock or inside the
81 magnetosheath itself.

82 Most magnetopause observations during radial IMF have noted a large magnetopause
83 expansion that was connected with a significant distortion of the magnetopause surface.
84 Large magnetopause distortion and anomalous sunward magnetosheath flows were reported
85 in one radial IMF event by (Shue et al., 2009). The finding of magnetopause displacement
86 during radial IMF conditions was also documented in a statistical study based on a large set
87 of magnetopause crossings using THEMIS (Dušík et al., 2010) and GOES (Park et al., 2016).
88 A systematic increase of observed magnetopause distances for radial IMF was found, ranging
89 from $0.3R_E$ at 90° cone angle to $\approx 1.7R_E$ at 0° or 180° cone angles compared to empirical
90 models. In contrast, using THEMIS data and empirical models of the MP, Grygorov et al.
91 (2017) concluded that the distance of the equatorial magnetopause is strongly affected by
92 radial IMF, expanding globally and independent of the local time, upstream value of other
93 solar wind parameters or the tilt of the Earth magnetic dipole.

94 It is interesting to remark that no self-consistent model exists today in the literature that
95 can explain the observed MP displacement or its asymmetry, particularly with the difficulty
96 MHD approaches have to accurately model reflected SW ions in the foreshock region (Sibeck
97 et al., 2001). In a recent study, (Samsonov et al., 2017) used previous statistical results to
98 suggest that the density and velocity in the foreshock region decrease to $\sim 60\%$ and $\sim 94\%$
99 of the undisturbed SW values when the cone angle falls below 50° causing a drop in the
100 SW dynamic pressure of $\sim 53\%$ that might cause the MP displacement. In a second step,
101 those authors modified the upstream SW parameters in a global MHD model to take these
102 foreshock effects into account, which helped them predict MP distances during non-radial

103 IMF intervals close to those observed by THEMIS. More precisely, using time dependent SW
104 conditions provided by ACE and WIND measurements in their simulations, they applied
105 a $\sim 53\%$ dynamic pressure reduction as soon as the SW cone angle becomes smaller than
106 50° . This limit was chosen in order to smooth the swap between radial (reduced dynamic
107 pressure) and non-radial (unchanged dynamic pressure) regimes (Samsonov et al., 2017). In
108 the present study, we employ constant upstream SW conditions. For the sake of covering
109 the full range of cone angles considered in the simulations of (Samsonov et al., 2017), we
110 have performed simulations for the two limit cases of 0° (referred to as radial IMF) and
111 $\sim 50^\circ$ cone angle (referred to as non-radial IMF). We note that there is no consistent usage
112 in the literature of the terms radial or quasi-radial IMF.

113 According to (Samsonov et al., 2017), the strong total pressure decrease in the data
114 seems to be a local, rather than a global, phenomenon. Those authors conceded that
115 their model was not self-consistent in the sense that the modified upstream SW parameter
116 adjustment was global and not specific to the foreshock region for which the statistical results
117 (discussed above) were initially derived. One of the goals of this study is to investigate the
118 role of backscattered ions in producing decreased SW pressure at the bowshock by resolving
119 them in a 3D kinetic simulation.

120 In addition to the expansion of the MP, the other focus of this study is the gener-
121 ation of dawn-dusk asymmetry under radial IMF, which has been investigated for many
122 decades (Akasofu et al., 1982; Akasofu, 1991; Haaland et al., 2017, and references therein).
123 Dawn-dusk asymmetries are ubiquitous features of the coupled solar wind-magnetosphere-
124 Ionosphere system. During the last decades, increasing availability of satellite and ground-
125 based measurements has made it possible to study these phenomena in more detail (e.g.,
126 B. M. Walsh, 2017). Most studies reported so far agree that the dawn-dusk asymmetry
127 is primarily the result of the Parker spiral solar wind impinging with a specific geometric
128 configuration that impacts and preconditions the magnetosphere (e.g., Haaland et al., 2017,
129 and references therein). Under radial IMF conditions, one would then expect the Parker

130 spiral effect to disappear while other physical processes, like kinetic effects, would drive any
131 dawn-dusk asymmetry. For instance, statistical studies based on THEMIS and Cluster mea-
132 surements confirm a rather global expansion of the magnetopause under radial IMF without
133 significant dawn-dusk asymmetries detected (Zhang et al., 2019). The same statistical study
134 showed that magnetic reconnection (MR) is nearly absent during radial IMF, in contrast
135 to the north IMF conditions during which MR and the consequent dawn-dusk asymmetries
136 are strong (Zhang et al., 2019).

137 Kinetic effects are expected to trigger a large set of distinct dawn-dusk asymmetries up-
138 stream of the magnetosphere due to the formation of the foreshock region that is connected
139 with solar wind particles backscattered at the bow shock. Although much of the plasma
140 passes through the bow shock, the reflected population generates a number of plasma insta-
141 bilities, which trigger waves and generate wave-particle interactions as well as other dynam-
142 ics at the non-parallel shock that should favor dawn-dusk asymmetries (e.g., B. M. Walsh,
143 2017, and references therein). The radial IMF condition would thus be the ideal configura-
144 tion to reveal such kinetic effects and determine their role in producing the dawn-dusk
145 asymmetry so far observed (Zhang et al., 2019). For reference, using Cluster single/multiple
146 spacecraft measurements, Haaland et al. (2014) discussed the dawn-dusk asymmetry at the
147 flanks and at the dayside MP. Similar results were also reported by Haaland et al. (2019),
148 as observed by two of the THEMIS spacecraft, showing the magnetopause being thicker on
149 dawn ($\sim 14\lambda_i$, λ_i being the ion inertial length) than on dusk ($\sim 8\lambda_i$), however no radial
150 IMF conditions were included in the statistical study. Additionally, other observations from
151 INTERBALL-1 and MAGION-4 spacecraft revealed asymmetry and deformation at the tur-
152 bulent magnetopause (Šafránková et al., 2000). Using Geotail observations for northern and
153 southern IMF, Wang et al. (2006) thoroughly discussed the dawn-dusk asymmetry in ion
154 density and temperature based on equatorial distribution of plasma sheet ions.

155

156 To interpret the magnetopause motion and the dawn-dusk asymmetry, many sophisti-
 157 cated models have been utilized, ranging from MHD to hybrid simulations. Early theoretical
 158 studies showed a contrast of 10%-20% between dawn and dusk bulk plasma properties (e.g.,
 159 Němeček et al., 2002; B. M. Walsh et al., 2012), however, those MHD-based models do not
 160 explicitly resolve kinetic effects, particularly at the foreshock region. For instance, using
 161 a global hybrid model (kinetic ions and fluid electrons), Blanco-Cano et al. (2009) studied
 162 radial IMF ($\theta_{vB} = 0$) impact on the solar wind interaction with the Earth's magnetosphere.
 163 The study focused on the micro-physics processes and wave-particle interactions in the fore-
 164 shock region but briefly mentioned the dawn-dusk asymmetry issue. Three other models i.e.
 165 hybrid, Hall-less and Hall-MHD simulations have been tested in one study by Karimabadi
 166 et al. (2004) for the analysis of MR regimes with the conclusion that dawn-dusk asymmetry
 167 is obtained and should be related to ions flow. Recently, Turc et al. (2020) used the hybrid
 168 -Vlasiator 2D-3V code to study asymmetries in the Earth magnetosheath for different IMF
 169 conditions. For reference, the Vlasiator code provides a kinetic description of ions, solv-
 170 ing directly the Vlasov equation for the particle distribution function in 2D-3D space, but
 171 assumes a fluid description for electrons (e.g. Palmroth et al., 2018). The authors report
 172 asymmetries larger than observed for the magnetic field strength, the plasma density, and
 173 bulk velocity, a discrepancy that was attributed to using a single set of upstream conditions
 174 in their simulations. It is interesting to remark that those authors obtained a stronger asym-
 175 metry for magnetic field strength when IMF gets closer to the radial configuration. However,
 176 it was not clear how the 2D spatial assumption and the fluid description of electrons in their
 177 simulations affected the reported magnetosheath asymmetries.

178 Based on the discussion above, two important questions appear: 1) what happens to
 179 the magnetopause shape, size, and location if flow-aligned IMF is applied to the system
 180 when kinetic effects are included for all species? and 2) does this generate asymmetry in
 181 the dawn-dusk and south-north directions? So in the dayside magnetosphere?

182 To answer these questions, we undertake a modeling study utilizing IAPIC, a particles-
 183 in-cell code (discussed in section 2). Our strategy is to be able to follow ions and electrons
 184 self-consistently with the Maxwell equations describing the fields. Thus the full range of
 185 collisionless plasma physics is captured for the macro-ions and macro-electrons involved in
 186 IAPIC, yet with limitations due to the grid spatial resolution and assumptions made on the
 187 plasma properties (particles density, ion/electron mass ratio, etc.) that we carefully discuss
 188 in section 2 (see Blanco-Cano et al., 2006; Eastwood, 2008; Jacobsen et al., 2009; Brackbill,
 189 2011; Masters et al., 2013; Ben-Jaffel & Ballester, 2014; S. Baraka, 2016). We adopt the
 190 initial and the boundary conditions reported in (Suvorova et al., 2010; Samsonov et al.,
 191 2017), we used single physical units for each parameters that were used in CCMC reported
 192 in (Samsonov et al., 2017).

193 This paper is structured as follows. This section has introduced the impact of radial
 194 IMF orientation on the dynamics of the Earth’s magnetosphere and presented a brief survey
 195 of observations of asymmetry in planetary magnetospheres. Two IMF orientations, namely,
 196 radial IMF ($B = B_x$) and non-radial IMF (B_x & $B_y > B_z$) will be covered in the current
 197 study.

198 In section 2, we describe the IAPIC code in details. The scaling of plasma parameters
 199 is also presented and tabulated.

200 In section 3, we show our findings regarding the magnetopause motion and the magne-
 201 tosheath asymmetry, an opportunity to compare to previous modeling results and obser-
 202 vations. In section 4, we discuss in details about the impact of the purely and non-radial
 203 IMF on the dynamics of the Earth’s magnetosphere, in light of the results obtained so far.
 204 In section 5, we present a summary of our findings and future related work.

2 Initial conditions and Simulation Model: IAPIC

2.1 Simulation Model: IAPIC

We use the Institut d’Astrophysique de Paris-Particle-In-Cell EM 3D global code (IAPIC) for treating the plasma kinetically. IAPIC has previously been applied to simulate various magnetospheres in the solar system (S. Baraka & Ben-Jaffel, 2011; Ben-Jaffel & Ballester, 2013, 2014; S. Baraka, 2016). IAPIC handles the equations of motion for large number of macro-particles (macro-ions and macro-electrons) self-consistently under the direct impact of electromagnetic fields through Lorentz force law (S. Baraka & Ben-Jaffel, 2007; Artemyev & Zelenyi, 2012).

The code was originally written by (Buneman et al., 1992) which used the boundary conditions reported in (Lindman, 1975) and charge conserving conditions as described in (Villasenor & Buneman, 1992). we use physical units for each parameter from (Samsonov et al., 2017) and scaled them to IAPIC values using a transformation matrix to convert GSM coordinates to the IAPIC code coordinates (see Fig. 1) as reported in (Cai et al., 2003). The solar wind parameters are normalized to spatial and temporal parameters and tabulated in Table 1 for radial IMF and Table2 for non radial IMF (see also, Table 1, Cai et al., 2015).

We follow the evolution of the fields and particles within a $61 \times 45 \times 45 R_E$ domain with Earth centered and $20 R_E$ downstream of the sunward (inlet) side (Table 1). We chose time step $\Delta t = 3700$ as our comparison point which corresponds to 24 minutes of real time (approximately twice the SW transit time) after starting the simulation. Each time step is equivalent to ≈ 0.38 sec and the spatial resolution of the code is $0.2 R_E$. We track 7.0×10^7 particle pairs, with an ion to electron mass ratio of 64.

Our normalized solar wind parameters to temporal and spatial values for both IMF orientations are given in Tables 1 and 2 for radial and non-radial IMF, respectively. The parameters are set such that a consistent initial conditions are validated before the code run

231

starts, denoted as $\Delta t = 0$, and at the step time, where the current study is considered i.e. $\Delta t = 3700$. These two tables are compared to similar study by (Cai et al., 2015)

Step time		$\Delta t = 0$		$\Delta t = 3700$	
Species/Parameters	Normalization	ions	electrons	ions	electrons
Thermal velocity, $V_{thi,e}$	$\tilde{v}_{thi,e} = \frac{v_{thi,e}}{\Delta/\Delta t}$	0.177	0.708	0.135	1.069
Debye length, $\Delta_{i,e}$	$\tilde{\lambda}_{i,e} = \frac{v_{thi,e}}{\omega_{pi,e}}$	0.8	0.4	0.52	0.52
Larmor radius, $\lambda_{i,e}$	$\tilde{\rho}_{ci,e} = \frac{\tilde{v}_{thi,e}}{\tilde{\omega}_{ci,e}}$	8.85	0.49	45	2.6
Gyro-frequency $\omega_{ci,e}$	$\tilde{\omega}_{ci,e} = \omega_{ci,e} \cdot \Delta t$	0.02	1.425	0.003	0.41
Plasma-frequency $\omega_{pi,e}$	$\tilde{\omega}_{pi,e} = \omega_{pi,e} \cdot \Delta t$	0.22	1.77	0.27	2.14
Temperature, $T_{i,e}$	$\tilde{T}_e = 2\tilde{v}_{the}^2, \tilde{T}_i = 2\tilde{v}_{thi}^2 \frac{m_i}{m_e}$	4.	1.	2.33	2.28
Gyroperiod	$\tilde{\tau}_{ci,e} = \frac{2\pi}{\tilde{\omega}_{ci,e}}$	314.15	4.4	2094.34	15.32
Inertial length $d_{i,e}$	$\tilde{d}_{i,e} = \frac{\tilde{c}}{\tilde{\omega}_{pi,e}}$	2.27	2.82	1.89	0.23

Unitless values

Step time	$\Delta t = 0$	$\Delta t = 3700$
Sound speed C_s	0.045	0.050
Alfvén speed v_A	0.050	0.012
Alfvén Mach number M_A	2.83	5.4351
Sonic Mach number M_s	3.16	1.3
Magnetosonic Mach number M_{ms}	2.0	1.27

Loaded Simulation Box Information

grid size	$\Delta = 0.2R_E = \Delta x = \Delta y = \Delta z$
Time Step	$\Delta t = \Delta_x/\Delta v = 7.08$
Simulation box size	$(305 \times 225 \times 255)\Delta$
# of pair-particles	7×10^7 ion/electrons pairs
Ion to electron mass ratio	64
Particle density	$n_i = n_e = 4/\Delta^3$

Table 1. Normalized solar wind parameters at the initial state and after 3700 Δt in the solar wind for both ions and electrons for radial IMF.

232

Step time		$\Delta t = 0$		$\Delta t = 3700$	
Species/Parameters	Normalization	ions	electrons	ions	electrons
Thermal velocity, $V_{thi,e}$	$\tilde{v}_{thi,e} = \frac{v_{i,e}}{\Delta/\Delta t}$	0.177	0.708	0.127	1.027
Debye length, $\lambda_{Di,e}$	$\tilde{\lambda}_{i,e} = \frac{v_{thi,e}}{\omega_{pi,e}}$	0.8	0.4	0.529	0.52
Larmor radius, $\lambda_{i,e}$	$\tilde{\rho}_{ci,e} = \frac{\tilde{v}_{thi,e}}{\tilde{\omega}_{ci,e}}$	3.175	0.29	25.4	1.95
Gyro-frequency $\omega_{ci,e}$	$\tilde{\omega}_{ci,e} = \omega_{ci,e} \cdot \Delta t$	0.04	2.435	0.005	0.525
Plasma-frequency $\omega_{pi,e}$	$\tilde{\omega}_{pi,e} = \omega_{pi,e} \cdot \Delta t$	0.22	1.77	0.24	1.955
Temperature, $T_{i,e}$	$\tilde{T}_e = 2\tilde{v}_{the}^2, \tilde{T}_i = 2\tilde{v}_{thi}^2 \frac{m_i}{m_e}$	4.010	1.0	2.065	2.109
Gyroperiod	$\tilde{\tau}_{ci,e} = \frac{2\pi}{\tilde{\omega}_{ci,e}}$	157.27	2.58	1256.63	11.960
Inertial length $d_{i,e}$	$\tilde{d}_{i,e} = \frac{\tilde{c}}{\tilde{\omega}_{pi,e}}$	2.27	0.282	2.08	0.255
Unitless values					
Step time	1	3700			
Sound speed C_s	0.04	0.035			
Alfvén speed v_A	0.085	0.017			
Alfvén Mach number M_A	1.65	2.855			
Sonic Mach number M_s	3.16	1.424			
Magnetosonic Mach number M_{ms}	1.463	1.272			
Loaded Simulation Box Information					
grid size		$\Delta = 0.2R_E = \Delta x = \Delta y = \Delta z$			
Time Step		$\Delta t = \Delta_x/\Delta_v = 7.08$			
Simulation box size		$(305 \times 225 \times 255)\Delta$			
# of pair-particles		7×10^7 ion/electrons pairs			
Ion to electron mass ratio		64			
Particle density		$n_i = n_e = 4/\Delta^3$			

Table 2. Normalized solar wind parameters at the initial state and after 3700 Δt in the solar wind for both ions and electrons for non-radial IMF.

2.2 Initial conditions

In IAPIC, the spatial and temporal scales (mass ratio and charge to mass ratio, etc ...) are chosen in order to be able to regenerate MHD large-scale classical structure of the Earth's magnetosphere (e. g., Omidi et al., 2004). For their modeling, Samsonov et al. (2017) used MHD and Community Coordinated Modeling Center (CCMC) resources, while the observational data are obtained from ACE, THEMIS and WIND spacecraft. Samsonov et al. studied the impact of non radial IMF on the magnetopause size and shape. Contextually, in the current study, we used the physical parameters they used in their MHD initial conditions and scaled them to the IAPIC initial condition values not only for non-radial IMF (where

242 B_x and B_y are dominant over B_z), but also for purely radial IMF (where B_y and B_z are
 243 absent). The radial IMF is an additional case included to study differences and similarities
 244 with the non radial nature of IMF on both magnetopause's shape and size and their role in
 245 creating dawn-dusk asymmetries. The initial conditions of Samsonov et al. (2017) and our
 246 two IMF orientations are then tabulated in Table 3.

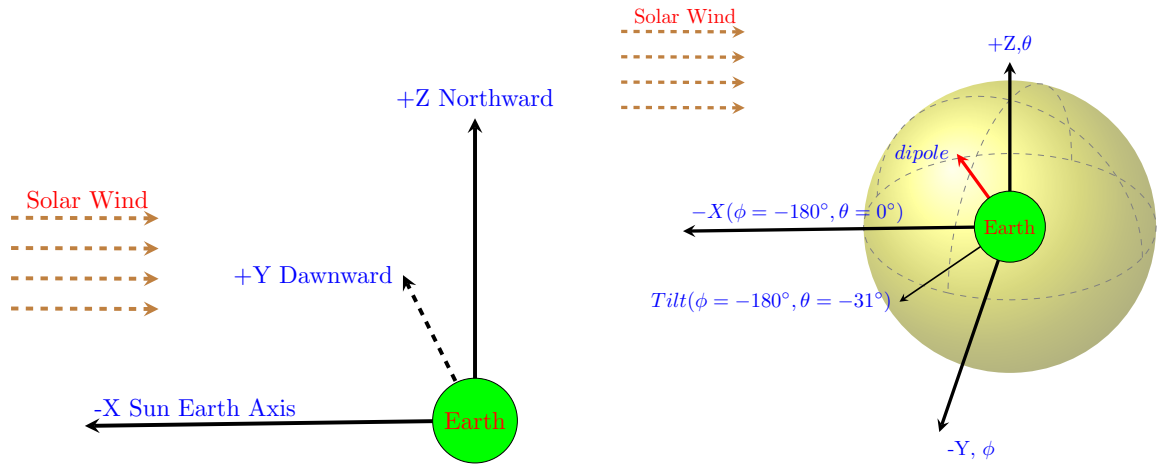


Figure 1. Code coordinates scheme (left) and spherical coordinates illustration used in MP derivation(right)

Table 3. MHD initial conditions and their corresponding IAPIC scaled values for radial and non-radial IMF orientation(Samsonov et al., 2017).

Parameters	Physical Units		Normalized Units	
	MHD	IAPIC _{radial}	IAPIC _{non-radial}	
N_{SW} (n/cc)	2.606	4.	4.	
T_{sw} (Kelvin)	32263	5×10^{-4}	5×10^{-4}	
V_x (km/s)	-470.69	0.1412	0.1412	
V_y (km/s)	-7.80	0	0	
V_z (km/s)	-5.0909	0	0	
IMF _{x} (nT)	-2.2	0.25	0.25	
IMF _{y} (nT)	2.99	0	-0.34	
IMF _{z} (nT)	0.659	0	0.075	
Tilt angle	31°	31°	31°	
Initial Cone Angle(θ_{Bx})	54°	0°	54°	
Initial Clock Angle(θ_{CA})	77.6°	45°	77.6°	

247 3 Simulation Results

248 To our knowledge, a full 3D global kinetic modeling of radial IMF impacts on the
249 dynamics of the magnetosphere has not been published, though the backstreaming of ions
250 in the solar wind flow has been theoretically discussed (e.g., Willis, 1978, Eq. 3). The non-
251 radial IMF event on July, 16th, 2007 observed by the THEMIS probes was chosen because
252 it has been the subject of several detailed studies (Jelínek et al., 2010; Suvorova et al.,
253 2010; Samsonov et al., 2017). The solar wind parameters and initial conditions were scaled
254 for IAPIC as described in section 2. For purposes of comparison, we discuss in detail the
255 plasma properties at the time step $3700\Delta t$ of our simulation for both full and non-radial
256 IMF. This time step corresponds to ≈ 24 minutes of real time, a relatively long enough
257 period to perform kinetic simulation of the dayside magnetosphere. In the following, IAPIC
258 simulation results are analyzed to determine the magnetopause shape, size and location for
259 the two IMF conditions assumed, which give us a good frame to characterize any dawn-dusk
260 asymmetry in the system.

3.1 Magnetopause response to radial and non-radial IMF

We derive the magnetopause's size to be the location of the vertical cut of the maximum density gradient steepening (using the number density derivative to get the maximum steepening). (e.g., Garcia & Hughes, 2007; J. Lu et al., 2015). We also use the pressure balance method to derive the MP location, a technique that offers an opportunity to explicitly include kinetic effects. Basically, in the pressure balance method, the dynamic and thermal pressures counter balance the dipole magnetic pressure. Because of the magnetic field axis tilt 31° at the time of observation, the system is inherently asymmetric and the Cartesian grid used in the IAPIC simulations is not adequate to accurately derive a density gradient in most planes, particularly in the tilted magnetic equatorial plane. To overcome this difficulty, we transform our Cartesian 3D simulation box quantities (density, velocity vector, ...etc, at (x,y,z) positions) into a spherical 3D domain (same quantities at (r, θ, ϕ) positions), at the price of losing data from regions outside a spherical volume of radius equal to the smallest dimension of the initial Cartesian box (Dusk-Dawn and South-North in our case). Our study does not suffer of that limitation because the dayside MP, our region of interest, is located inside the selected spherical domain. After checking that both reference frames provide the same spatial distribution of all physical quantities along Sun-Earth(OX), Dusk-Dawn(OY), and South-North (OZ) axis, we focus on deriving the magnetopause size at two key planes, namely the magnetic tilt plane $\theta = -31^\circ$ and the plane $\theta = 0^\circ$ that contains the Sun-Earth line.

To quantify the MP expansion, we applied Shue model (Shue et al., 1997) on our physical units initial solar wind conditions, finding a MP size equal $10.3 R_E$. Therefore, this size will be used as the reference MP length in the current study. Our findings are summarized and tabulated in Table 4.

In a first step, we focus on the direction defined by $\phi = -180^\circ$ in both planes. Using the maximum density steepening technique, we derive comparable values for the magnetopause position at $(\sim 10.6, \sim 11.0) R_E$ respectively for radial and non-radial IMF along Sun-Earth

288 line. We also obtain the same size when the effect of backstreaming ions is removed from
 289 the bulk flow. However, along the tilted axis contained in the magnetic tilt plane, the
 290 magnetopause positions are (11.6, 12.0) R_E with bulk flow, which also remain unchanged
 291 without backstreaming ions, respectively for the two IMF conditions.

292 First, we note that the different magnetopause positions derived from the IAPIC sim-
 293 ulation are all larger than the expected magnetopause position ($\sim 10.3 R_E$) derived from
 294 Shue model (Shue et al., 1997). We remind that this reference MP size corresponds to
 295 the initial solar wind physical parameters used in our simulations. All values derived show
 296 an expansion of the magnetopause position along the two selected axes but also sunward.
 297 The magnetopause appears to be subjected to a reduced SW pressure that allows the dipole
 298 magnetic field network to expand outward. Based on the maximum density steepening tech-
 299 nique, it is remarkable that our model predicts the magnetopause expansion self-consistently
 300 in the range (0.7-1.7) R_E along Sun-Earth axis and magnetic tilt axis for non-radial IMF.

301 In the following, we explore our 3D IAPIC simulation results to try uncovering potential
 302 processes that could be at the origin of the measured expansion. Since early reports, several
 303 studies pointed to the potential impact of kinetic effects, particularly with the detection of
 304 the signature of particles streaming in a direction opposite to the solar wind (Spreiter &
 305 Alksne, 1969; Willis, 1978; Sibeck et al., 2001; Samsonov et al., 2017). As IAPIC simulations
 306 offer the access to all populations of particles (macro-particles) with specific kinetic proper-
 307 ties, we tried to extract those particles on the dayside that move sunward, against the main
 308 impinging solar flow. That statistical sub-population of particles has its own kinetic prop-
 309 erties and most importantly counterbalances the ram pressure of the incident solar flow, as
 310 if it was originating from the magnetosphere and flowing outward. It is important to stress
 311 that this population has kinetic properties (temperature, speed, etc) much different from
 312 the planetary ionospheric population that flows from the plasmasphere or the polar wind.
 313 In Fig.2, bulk pressures (dynamic, thermal denoted P_{dyn} and P_{thm} respectively) are shown
 314 with and without backstreaming ions to highlight the difference they make in the pressure

315 balance. First, we remark that the thermal pressure is dominant over dynamic pressure in
 316 the magnetosheath. P_{dyn} and P_{thm} cross P_{mag} at two points, i.e. with and without back-
 317 streaming ions included. The corresponding size of the MP is $10.8R_E$ for radial IMF and
 318 $11.7R_E$ for non-radial IMF along the Sun-Earth axis. Importantly, if the backstreaming ion
 319 effect is removed, then the magnetopause size drops down to 10.5 and $11.4R_E$ for same IMF
 320 orientations respectively. The magnetopause is also measured along the tilted magnetic axis
 321 with and without backstreaming ions and found equal to 11.9 , $11.5R_E$ for radial IMF and
 322 12.0 , $11.6R_E$ for non-radial IMF, respectively. To summarize, these findings are tabulated
 323 in Table 4. It is worth notice that the expansion ranges when using the pressure balance
 324 method for deriving the MP size is slightly different from that using the density steepen-
 325 ing method. For example, The MP expansion rate is 0.5 - $1.4R_E$ for radial and non-radial
 326 IMF along Sun-Earth axis, compared to 0.3 - $0.7R_E$ derived by maximum density steepening
 327 method. The difference between the two measurements is 0.2 - $0.7R_E$. The expansion range
 328 is 1.6 - $1.7R_E$ as derived by pressure method compared to 1.3 - $1.7R_E$ as measured by density
 329 steepening method respectively along tilted magnetic axis. With only a difference between
 330 the two methods of $0.3R_E$ for radial IMF and similar values for non radial IMF along the
 331 tilted magnetic axis.

332 In their papers (Bonifazi & Moreno, 1981b, 1981a) used ISEE2 data of 3253 ion spectra
 333 that corresponds to ≈ 90 hours, studying the density and energy of the backstreaming ions.
 334 They quantitatively characterized them into three categories. The authors used a scaling
 335 factor such that the ratio (A) of the backstreaming bulk speed to their thermal speed is
 336 ≥ 1.2 for reflected ions, and ≤ 0.8 for diffuse ions with an intermediate case $0.8 \leq A \leq 1.2$.

337 Here, we adopted their method to quantify the characteristics of the backstreaming ions
 338 in the dayside solar wind flow. First, a simple statistical study of the dayside populations
 339 shows that 16.5% and 20% of the solar wind bulk flow are backstreaming. For the radial
 340 IMF, we found that 72.5% of backstreaming ions are characterized by the factor $A > 1.2$,
 341 i.e. are reflected ions along the OX axis. However, only 27.5% of backstreaming ions can

Maximum Density Steepening magnetopause derivation

IMF /Axis	Sun-Earth Axis		Tilted Magnetic equator axis	
	Yes	No	Yes	No
Kinetic effects	Yes	No	Yes	No
magnetopause for radial IMF	10.6 R_E	10.6 R_E	11.6 R_E	11.6 R_E
magnetopause for non radial	11.0 R_E	11.0 R_E	12.0 R_E	12.0 R_E

Pressure balance magnetopause derivation

IMF/Axis	Sun-Earth Axis		Tilted Magnetic equator axis	
	Yes	No	Yes	No
Kinetic effects	Yes	No	Yes	No
magnetopause for radial IMF	10.8 R_E	10.5 R_E	11.9 R_E	11.5 R_E
magnetopause for non radial	11.7 R_E	11.3 R_E	12. R_E	11.6 R_E

Table 4. Summary of results are tabulated as derived by density steepening method (derivative of number density) and pressure balance methods for both IMF orientations. The values are measured on both Sun-Earth Axis and magnetic tilted axis. The kinetic effect is when the bulk flow is considered, and its absence when inflow only is considered. The reference size for these values is $10.3R_E$.

342 be characterized as intermediate ($0.8 < A < 1.2$). see Fig. 9-(a). For the non-radial IMF
 343 case, we found a totally different characteristics for the backstreaming ions. There are only
 344 21.6% reflected particles, and 31.4% intermediate particles and 47.0% diffuse particles along
 345 the same OX axis. To follow up the impact of the tilt axis on the particles populations, we
 346 also conducted the same statistical analysis on the magnetic equator tilt axis. We found for
 347 radial IMF that 59% reflected ions and 41% in the intermediate phase. On the other hand,
 348 the backstreaming ions are characterized as 23.5% for reflected ions, 53% for intermediate
 349 case, and finally 23.5% for diffuse ions. In Fig. 9 we found that for radial IMF, on both
 350 axis, most of the backstreaming ions are in the reflection mode, with small percentage in
 351 intermediate mode at the bow shock. On the other hand, for non-radial IMF, on both axis,
 352 backstreaming ions are in intermediate and diffuse mode in the solar wind, but the reflection
 353 mode appears to be dominant around the bow shock.

354 In the following, we track the magnetopause shape for both IMF orientations in two
 355 different locations. In order to handle the complex geometry of the tilted dipole, we use
 356 spherical coordinates such that $\phi = -180^\circ$ at the dayside standoff distance, ($\theta = 0$) along Sun-
 357 Earth Axis and ($\theta = -31$) along the magnetic tilt axis. In that frame, we track the shape every
 358 20° along ϕ in two different axes (e.g., Fig.3). The MP shape for the two IMF orientations is
 359 constructed in the XY-plane and in the magnetic equator that both contain the dusk-dawn
 360 direction. In Fig.3, the MP is shown in the half-plane that contains dawn (positive Y), so
 361 that the asymmetry between dusk and dawn clearly appears using a mirror image of the
 362 MP shape in the dusk half-plane that is over-plotted on the dawn half-plane. For example,
 363 Fig.3 (a) and (b) show clear dusk-dawn asymmetry for the two selected planes (i.e. XY and
 364 magnetic equator planes). It is noticeable that the size of the MP shape strongly extends
 365 up to $\approx 15R_E$ along both dusk and dawn directions.

366 On the other hand, for non-radial IMF, the MP shape is shown in panels (c) and (d).
 367 The MP shape in panel (c) is squeezed earthward in dawn direction down to $7.5R_E$ with a
 368 dynamic nature structure of this portion of the MP. It is reasonable to anticipate that this
 369 reduction of the size in dusk-dawn is attributed to the strong impact of B_y . While the dusk
 370 portion of the MP shows clear asymmetry with spread out length of $\approx 12R_E$. In Fig.3 (d),
 371 we have a peculiar quasi-symmetric MP shape in the magnetic equator with a size $\approx 11R_E$
 372 on down/dusk. We don't exactly know why this shape takes this form, but we suspect dual
 373 effects between B_y and the strong plasma current sheet that originates in the magnetotail.
 374 It seems that B_y pressuring the boundary of the MP on the flanks are encountering the
 375 pressure of the current sheet at the tilted magnetic axis. This effect is absent in the radial
 376 IMF.

377 In Fig.4, the linear densities for both IMF orientations are plotted in three different
 378 directions. For purely radial IMF Fig.4-a, ions and electrons are over-plotted along Sun-
 379 Earth line (OX-upper panel) from -20 to $-10R_E$ measured at $Y=Z=0$, Dusk-Dawn line(OY-
 380 middle panel) from -20 to -20 measured at $X=12R_E$ and $Z=0$, and South-North line(OZ-

381 lower panel) measured at $X=12 R_E$ and $Y=0$. Densities in OY, and OZ panels are aimed
 382 to show the density profile just outside the MP position take at $-12R_E$. Vertical dashed line
 383 in the upper panel shows where the densities are plotted in the other two directions. Fig.4
 384 shows the quasi-neutrality of the solar wind. The ions and electrons are correlated with no
 385 charge separation. Also, it is found that along OY and OZ taken just outside the MP there
 386 is apparent asymmetry at both dusk-dawn and south-north direction.

387 Similarly for non-radial IMF is plotted in Fig.4-b, in the OX plane, we notice a
 388 hump/heap just outside the bow shock at $\approx -16R_E$. We track plasma backstreaming
 389 at that distance and only little fraction is noticed. Its nature is reflection, in according to
 390 the characterization of backstreaming ions reported in Fig. 9. The plasma jump at $-16R_E$
 391 is factor 2 that is noticed when we plot the linear density along OY and OZ (not shown in
 392 the plots).

393 The linear density along Dusk-Dawn shows the asymmetric boundary layer structure
 394 with higher density on the dawn side than on the dusk side while in the South-North direc-
 395 tion the linear density shows a high peak of plasma of 1.5 times higher in the south region
 396 than in the northern one.

397 The other major components of the solar wind dynamics is its velocity modulus that is
 398 shown in Fig.5 in the same order. The density hump in Fig. 4-b corresponds a velocity
 399 decrease in the corresponding sub-figure in Fig.5-b.

400

401 To better visualize asymmetries on large scales of the system, contour plots show a 2D
 402 cut of the plasma density distribution and magnetic field topology in 3 planes as shown in
 403 Fig.7 & 6. It is found that the planet tilt (31°) has a major impact on the global macro-
 404 structure of the magnetosphere in the simulation box of size ($\approx 60 \times 40 \times 40 R_E$). In Fig.7,
 405 panels a, b, and c are the 2D contour plot for plasma distribution along Sun-Earth axis,
 406 Dusk-Dawn axis, and South-North axis for radial IMF. Respectively panels d, e, and f are
 407 for non-radial IMF. In Fig.7-a, the planet tilt is clearly depicted. When the forefront of the

408 solar wind coplanar inflow approaches the magnetosheath, it hits the upper boundary of the
 409 magnetopause before the tilted magnetic axis, which makes the plasma override the bound-
 410 ary there before it reaches the lower boundary. This results in squeezing the magnetopause
 411 at high latitude and relaxes it in lower latitude thus making it flares out in the nightside at
 412 around $20R_E$ (see also Fig.3-a). There is around $6R_E$ vertical distance between the Sun-
 413 Earth and the tilted magnetic axes. Ionosphere is not included in the current study, while
 414 particles entry inside the magnetosphere is seen up to $5R_E$. The plasmasphere is shown up
 415 to $7R_E$. In Fig.7-d showing the plasma distribution for non-radial IMF, there is a plasma
 416 hump of $\approx 2.3R_E$ thickness between -17 and -14.5 along the Sun-Earth line and extended
 417 curve-linearly from -12 (south) to 7 (north) in a dome-like shape. It is not clear what
 418 causes this hump that is absent in the radial IMF case at the same time step. The dynamic
 419 pressure at both cusps is relatively equivalent contrary to the radial case. The relaxation
 420 of the southern part of the magnetosphere showed denser plasma population up to $30R_E$
 421 tailward and flared in toward north at around $25R_E$. The cavity around the planet position
 422 is smaller and more confined in the non-radial IMF than the radial IMF case.

423 Besides that, the 2D plasma distribution in the equatorial plane for radial IMF (Fig.7-b),
 424 shows the impact of the dipole tilt on the plasma distribution in both dusk and dawn direc-
 425 tions. It is found that the magnetosheath contracts under the pressure of large populations
 426 in the bow shock which is larger on the dusk side than on the dawn side. Furthermore,
 427 particle entry inside the magnetosphere is largely distributed around the planet making the
 428 cavity reaches $\pm 5R_E$ on South-North direction and around $3R_E$ tailward, with plasma tube
 429 along the Sun-Earth line up the planet position. While on the other hand, the effect of B_y
 430 for the non-radial IMF in Fig.7-e, shows the compressed magnetopause on both locations of
 431 dusk and dawn along OX and tilted magnetic axes. The cavity around the planet is more
 432 confined and reduced in size to $\pm 3R_E$ along south north and $\approx 1.4R_E$. The magnetospheric
 433 structure in the Dusk-Dawn plane for radial IMF (Fig.7-c) shows denser plasma in the dawn
 434 sector from 10 to $20 R_E$ than on the dusk side from -10 to $-20 R_E$, while in the northern
 435 sector of the magnetosphere there is a denser plasma that extends from around 10 to $17R_E$

436 but not regularly structured with same thickness in the southern sector. It appears that
 437 there is a finger like structure (particle entry) at around $5R_E$ on the dusk side that extends
 438 to around $1R_E$ in the cavity around the planet, on the other hand, for non-radial IMF the
 439 plasma distribution contour shows smaller cavity size and denser plasma on the dusk side,
 440 with a large plasma structure starting at $10 - 20R_E$ dawn and $10R_E$ north and extends to
 441 $20R_E$ downward (Fig. 7-f).

442 Furthermore, Fig.6 shows the corresponding magnetic field topology of Fig.7 respec-
 443 tively. This figure sheds light on the differences and similarities between two IMF orien-
 444 tations along three different planes. In Fig.6-a the radial IMF field lines along OX are
 445 horizontal at $-20R_E$ and $\pm 3R_E$ along South-North direction and seen curled at $\pm 10R_E$.
 446 At the magnetopause position, the field lines divert at $f(x,z)=(-10,-8)R_E$. At dayside
 447 magnetosphere, there are two potential magnetic reconnection sites(MR) sites approx-
 448 imately located at $f(x,z)=(0.5,-12)\&(-7.6,11.9)R_E$. The magnetic field line topology
 449 shown in Fig.6-d is horizontal in the undisturbed SW, this was not the case in Fig.6-a.
 450 This difference is attributed to the impact of B_y . Potential MR sites are seen also at
 451 $f(x,z)=(-10.6,9.1)\&(0.5,10.1)R_E$. Constant attention should be made when looking at
 452 Fig.6-b, taken in the equatorial plane, because of the dipole tilt, what is shown here for
 453 radial IMF is the high latitude magnetopause along OX in Dusk-Dawn direction. It is
 454 found that field lines from IMF connect to dipole field and permit particle entries at that
 455 latitudes. The wavy structure in the nightside (not the focus of the current study) indi-
 456 cates a complex current system induced at that distance. A potential MR site is shown
 457 at $f(x,y)=(-7.6,9.9)R_E$. The curling of magnetic field lines at $f(x,y)=(5,-15), (-15,-7)R_E$
 458 corresponds to the plasma dynamics shown in Fig.7-d. Same in Fig.7-e for non-radial IMF,
 459 the curled magnetic field lines at a latitude corresponding to $\approx 6R_E$ (north) are directed
 460 toward dusk-midnight direction. Potential MR sites are at $f(x,y)=(4.4,5.9), (-8.6,0.1), (3.5,-$
 461 $7.9)R_E$. In Fig.6-c, the dawn side magnetic field topology shows more extended structure of
 462 closed magnetic field lines until $\approx 14R_E$ toward dawn and reach up to $12R_E$ northward. In
 463 contrary, the non-radial IMF case in Dusk-Dawn plane (Fig.6-f) shows different structure,

464 where the extension of field lines is more important on the dusk side, but there are large
 465 scale connections of planetary and interplanetary magnetic field lines and clear MR position
 466 at $f(y,z)=(-9.6,9),(3.4,-11.4)R_E$.

467 The solar wind species temperature is important to track the particles entry from the
 468 cold component, the solar wind origin, to hot component of the magnetosheath plasma.
 469 The T_i/T_e is approximately conserved at the MP boundary. (Wing et al., 2014). Moreover,
 470 the T_i/T_e ratio is thoroughly investigated by (Lavraud et al., 2009) . In the current paper,
 471 the ion-to- electron temperature ratio (T_i/T_e) of the impinging solar wind is depicted in
 472 Fig.8. For radial IMF Fig.8-a, the ion temperature T_i slightly fluctuating in the solar wind
 473 until it increases by a factor 2 between -15 to-12 R_E then decreased downstream before
 474 it increased again in the magnetosheath until it reached the MP position before abruptly
 475 jumped inside the magnetosphere. While on the other hand the electron temperature T_e in
 476 the magnetosheath maintains constant value, with factor 1.2 than electron temperature in
 477 the solar wind. The average (T_i/T_e) ratio in the magnetosheath is ≈ 1.1 . Moreover the
 478 temperature profile in the non-radial IMF Fig.8-b. is different from that purely radial IMF.
 479 The T_i start constantly increasing at $-15R_E$ including the bow shock and the magnetosheath.
 480 The T_i ratio in the sheath to the solar wind is a factor 4. The T_e on the other hand,
 481 start increasing at $-16R_E$ up to downstream and continued inside the magnetosheath. The
 482 average (T_i/T_e) ratio in the magnetosheath is ≈ 2 . more discussion about temperature
 483 ion-to-electron ratio and temperature anisotropy is in section-(4)

484 The temperature anisotropy was studied extensively in the past(Gingell et al., 2015;
 485 Karimabadi et al., 2014; Treumann & Baumjohann, 2013). In the current paper, we were
 486 able to derive the solar wind species temperature anisotropy. In Fig.8-c for radial IMF,
 487 the average ion temperature anisotropy $T_{\perp i}/T_{\parallel i}$ in the dayside magnetosphere is ≈ 1.7 , and
 488 inside the magnetosheath this ratio reaches ≈ 2.7 , the maximum ratio is found at the bow
 489 shock with a factor of 3.3. It is found that the temperature anisotropy where the solar wind
 490 plasma departs their thermal equilibrium in the solar wind is almost isotropic. As per the

491 average electron temperature anisotropy $T_{\perp e}/T_{\parallel e}$, it is found in the dayside magnetosphere
 492 equal ≈ 2.2 which is almost the same inside the magnetosheath. In Fig. 8-d, for non-radial
 493 IMF orientation, the anisotropy average for ions in the dayside magnetosphere is $T_{\perp i}/T_{\parallel i}$
 494 ≈ 6 for ions and ≈ 1.6 for electrons. In the magnetosheath the $T_{\perp i,e}/T_{\parallel i,e}$ for ions and
 495 electrons is 3.2 and 3.4, respectively. These results will be discussed in section 4.

496 **3.2 Dawn-Dusk asymmetry in the dayside magnetosphere under the influ-** 497 **ence of radial and non-radial IMF**

498 . The large scales results reported above all indicate systematic asymmetries in Dusk-
 499 Dawn and South-North directions for the two IMF orientations. In the following, we try
 500 to quantify those asymmetries, particularly in the Dusk-Dawn direction for the radial and
 501 non-radial IMF cases we have simulated. Figures, 3, 4, 7-(panels, b, e, c, and f), and 11
 502 clearly show asymmetry in the Dusk-Dawn direction.

503 Fig.7-b,e show the Dusk-Dawn asymmetry along the Sun-Earth direction (OX) and
 504 Fig.7-c,f show the asymmetry along the Dusk-Dawn (OY) and South-North(OZ) directions.
 505 Linear density plots are shown in Fig.4, middle panel, and plasma boundary layers in the
 506 equatorial. The asymmetry in the South-North planes can be seen in Fig.4 lower panel. In
 507 Fig.11, some solar wind parameters i.e. N_i , T_i , T_e , V_i , B_x, B_y and B_z are plotted at three
 508 different locations for each IMF orientation. Two of which are at $\pm 6R_E$ on both sides of OX
 509 axis, and the third along the Sun-Earth line from -18 to 10.8 and $11.7 R_E$ for radial and
 510 non-radial IMF. More details are given in the next section 4. In Table 5 measured values of
 511 the solar wind parameters are tabulated.

512 In Fig.11, left panel shows the radial IMF parameters. Ion plasma is denser along OX
 513 in the dusk side than on the dawn side in the solar wind up to the magnetosheath. For
 514 non-radial IMF, right panel, density in the dusk side got a factor 2 jump in the bow shock
 515 region for the density in both dawn and along OX axis. For ion temperature T_i , we noticed
 516 that it is hotter in the dawn side only in the solar wind before the foreshock region, then it

517 cools down and the dusk temperature increases. The up and downstream ion temperature
 518 long OX is close to that along dusk for radial IMF. For non radial IMF, we noticed that
 519 there is hotter plasma in the solar wind along dusk direction. Then, T_i is correlated with the
 520 other directions, but still show asymmetry. On the other hand, T_e is hotter in the solar wind
 521 along dusk direction, and then cooles down in the downstream compared to that in the dawn
 522 and OX direction. Ion velocity (V_i), decelerates at both dusk and dawn directions though
 523 it is faster than V_i on OX direction for radial IMF. For non-radial IMF, the deceleration
 524 of solar wind in the downstream is correlated along OX and dusk direction but it s steady
 525 along dawn. For all parameters considered, there is an apparent dawn-dusk asymmetry.

Solar wind parameters for radial IMF

Parameter	Dawn ($Y = +6R_E$)	Dusk ($Y = -6R_E$)	OX ($Y=0$)	Dawn/dusk
N_i	8.148	8.076	7.978	0.988
T_i	0.003	0.004	0.007	1.704
T_e	0.156	0.192	0.218	1.132
V_i	0.054	0.043	0.038	0.878
B_x	0.226	0.105	-0.023	0.218
B_y	0.193	0.141	-0.216	1.532
B_z	-0.033	-0.067	-0.053	0.790

Solar wind parameters for non radial IMF

N_i	8.308	4.176	3.206	0.768
T_i	0.002	0.002	0.004	1.946
T_e	0.153	0.144	0.161	1.118
V_i	0.052	0.045	0.021	0.456
B_x	0.130	0.248	0.156	0.631
B_y	-0.442	-0.384	-0.462	1.202
B_z	0.003	0.152	-0.008	0.054

Table 5. To monitor the Dusk-Dawn asymmetry, plasma parameters are calculated and averaged at the derived position of the magnetopause at $10.8R_E$ at subsolar point, $8.5R_E$ at dusk flank, and $6R_E$ at dawn flank for radial measured at $\pm 6R_E$. While data is derived for non radial IMF as $11.7R_E$ at the subsolar MP, $8.6R_E$ at the dusk flank, and $6.9R_E$ at the dawn flank respectively.

526 4 Discussion and Analysis

527 As described in section 3.1, we derived the MP position (10.6,11.0) R_E along the Sun-
 528 Earth line for purely and non-radial IMF, respectively (using the location of the maximum
 529 number density gradient). In addition, we have shown that PIC simulations offer the pos-
 530 sibility to isolate backstreaming ions from the pool of particles in the box simulation. This
 531 process allows us to derive their contribution to the dynamic and thermal pressures in the

532 dayside magnetosphere. It is important to stress that other complex effects could be induced
 533 by the presence of those backstreaming particles, like induced currents and fields, that will
 534 be considered in a future study. Elimination of the contribution of backstreaming ions in
 535 the ensemble average of the plasma properties increases the resulting system pressure and
 536 consequently moves the magnetopause location toward Earth.

537 Using the balance between ram pressure and magnetic pressure, (e.g., Willis, 1978, Eq.
 538 3) we were able to derive the MP size in different planes with and without backstreaming
 539 ions (Table 4). These calculations reveal the impact of backstreaming ions in reducing the
 540 solar wind dynamic pressure allowing for MP expansion by $0.3-0.4R_E$. All our findings above
 541 also suggests the important results that by neglecting ions kinetic effects, MHD simulations
 542 implicitly overestimate SW pressure in the foreshock and underestimate the MP size.

543 For instance, the MP expansion range derived here is consistent with the expansion
 544 observed by THEMIS spacecraft for the event of July, 16th, 2007. To match the observed
 545 expansion, Samsonov et al. (2017) were forced to modify the solar wind properties, propa-
 546 gated from WIND and ACE *in situ* measurements, of their boundary conditions in order for
 547 their MHD model. This means that a non negligible fraction (up to 40%) of the observed
 548 expansion that is due to backstreaming particles was inadvertently attributed in their study
 549 to a change in the SW upstream properties.

550 We conclude that the dynamic pressure of backstreaming ions contributes significantly
 551 to the expansion/compression of the magnetopause. Note that when the magnetopause is
 552 derived from the density maximum steepening, the effect of the backstreaming ions was
 553 absent. This indicates that the main driver of the expansion of the magnetopause is the
 554 upstream reduction of the solar wind dynamic pressure in the foreshock. More generally, the
 555 insensitivity of the MP size to the density of backstreaming ions confirms the conclusions
 556 reported in (Samsonov et al., 2020, Eq. 2), that density and velocity (dynamic pressure)
 557 might have different contributions to the effective values of the dynamic pressure component
 558 in the pressure system balance used in driving the magnetopause position. This appears

559 clearly in our results in Table 4.

560

561 The presence of backstreaming particles should also affect the temperature anisotropy
 562 in the dayside magnetosphere. Using THEMIS measurements, (Wang et al., 2012) showed
 563 how the T_I/T_e ratio changes in the magnetosheath and the plasma sheet. They showed that
 564 $T_I/T_e \approx 4 - 12$ in the magnetosheath. Other studies statistically examined the T_i/T_e in
 565 different regions in the magnetosphere to find a ratio $\approx 6-12$ (Phan et al., 1994; Paschmann
 566 et al., 1993). On the other hand the T_I/T_e ratio was as low as ≈ 3 as reported in (Lavraud
 567 et al., 2009) when the authors studied this ratio at the flank magnetosheath. In the current
 568 paper, we show in Fig.8-a and (b), the ion and electron temperature ratio in the dayside
 569 magnetosphere. The average T_i/T_e ratio in the magnetosheath is found 1.7 and 1 for radial
 570 and non-radial IMF (Dimmock et al., 2014, 2015). The T_i/T_e ratio for non-radial IMF
 571 is ≈ 1 but it reached an average of 5 if taken from -18 to -10 R_E . On the other hand,
 572 (Grygorov et al., 2017; Samsonov et al., 2012) showed that the temperature anisotropy in
 573 the magnetosheath controls the pressure distribution near the magnetopause. Here we found
 574 that the ion temperature anisotropy ratio is about 2 in the magnetosheath for radial IMF,
 575 and about 6 for non radial IMF (Fig.8-c,d), consistent with (Wang et al., 2012). Analysis
 576 of the temperature distributions will be used in future work to study microinstabilities and
 577 reconnection.

578 To characterize the kinetic properties of the backstreaming particles, we first use the
 579 nomenclature of (Bonifazi & Moreno, 1981b). We found that for the radial IMF, the percent-
 580 age of reflected ions ($A > 1.2$) in the backstreaming population is 72.54%, while intermediate
 581 reflected ($0.8 < A < 1.2$) ions represents 27.45% (see Fig. 9-(a)). For the non-radial IMF
 582 case, we found that backstreaming ions have totally different characteristics as only 21.56%
 583 of them are reflected particles, 31.37% are intermediate particles, and 47.05% diffuse parti-
 584 cles. In Table 6 we show the speed of backstreaming bulk velocity in real physical units in
 585 accordance with the characterization factor reported in (Bonifazi & Moreno, 1981b). It is

586 found that the backstreaming ions are faster along the tilted magnetic axis than the sun-
 587 earth axis for both IMF orientations. It is the same case for the thermal speed of those
 588 ions. While the bulk flow speed is faster for radial IMF along the sun- earth line than the
 589 tilted magnetic axis, on contrary, the bulk flow speed is faster along tilted magnetic axis
 590 than the sun-earth axis for non-radial IMF. Note that 16.5% and 20% of the bulk flow are
 591 backstreaming ions for radial and non-radial IMF respectively.

592 To better understand the kinetics of the distribution of the backstreaming ions, we
 593 show the velocity distribution function (VDF) of solar wind ions along the Sun-Earth line
 594 as far as $-20R_E$ (Fig.10). For the purely radial IMF case, a substantial fraction of VDF
 595 spatial distribution of backstreaming ions is found in the three planes (XZ, XY and YZ)
 596 whereas only a small fraction is obtained for non-radial IMF especially in the YZ plane.
 597 The VDF in Fig.10-a shows reflection of the plasma sunward and southward for radial IMF,
 598 with minor reflection for non radial IMF with a lot of diffuse northward and earthward
 599 direction as confirmed by Fig. 9. It is also found that in the equatorial plane for both IMF
 600 orientations, that the reflection of backstreaming ions are dominant over their diffuse and
 601 intermediate for radial than non radial IMF. While on the other hand in Fig.10-c and f, the
 602 spatial distribution of ions are reflected mostly toward south and sunward for radial and
 603 mostly toward north for non radial IMF.

604 The second major finding of this study is the Dawn-Dusk asymmetry. Uncovering
 605 its origin is important for better understanding, modeling and prediction of space weather
 606 phenomena (e. g., S. Lu et al., 2016). Asymmetry is observed by Cluster spacecraft in
 607 north-south magnetotail planes (Haaland et al., 2017; Samsonov, 2006) and in dawn-dusk
 608 planes (A. P. Walsh et al., 2014; Samsonov, 2011; Dimmock et al., 2017; Turc et al., 2020).
 609 Both observations and numerical simulations have revealed that the magnetopause size is a
 610 function of IMF strength and orientation, and solar wind dynamic pressure, which by turn
 611 modify the magnetopause shape and generate dawn-dusk asymmetries (Liu et al., 2019).
 612 Using data from IMP 8 and ISEE,1, ISEE, 3 and WIND, Paularena et al. (2001); Dimmock

Number density data

	Radial	Non radial
# inflow ions	5.38958×10^7	5.21372×10^7
# backstreaming ions	8.87744×10^6	1.07256×10^7
percentage	16.5%	20%

Backstreaming Ions Characteristics

	Radial		Non radial	
	OX	Tilt	OX	Tilt
reflected ions	72. %	58. %	22. %	24. %
intermediate ions	27. %	41. %	31. %	53. %
diffuse ions	1. %	1. %	47. %	23. %
$V_{bp}(km.s^{-1})$	373	392	294	346
$V_{thm}(km.s^{-1})$	254	255	321	332
$V_{sw}(km.s^{-1})$	287	254	233	248

Table 6. The ratio of backstreaming ions to bulk flow of the number density for both IMF orientations is shown in the upper panel. The backstreaming ions are characterized with three categories (see Fig. 9). Based on scaling factor ((Bonifazi et al., 1980)) the backstreaming ions are reflected, intermediate or diffuse. V_{bp} bulk flow of the backstreaming ions, V_{thm} , their thermal speed and the solar wind velocity V_{sw} are shown in the lower panel for both IMF orientations along OX and Tilt axis.

613 et al. (2014) showed a significant dawn-dusk asymmetry in the Earth's magnetosheath which
 614 is larger on the dawn side than on the dusk side. They also showed that the IMF orientation
 615 impacts density asymmetry in dawn-dusk direction. Paularena et al. (2001) reported same
 616 kind of asymmetry in different regions in the dayside magnetosphere in Sun-Earth and
 617 Dusk-Dawn planes. In their recent study, Turc et al. (2020) discussed the magnetosheath
 618 asymmetry in terms of IMF, solar wind density, velocity by using Vlasiator hybrid code
 619 (Palmroth et al., 2018). They found that magnetic field asymmetry and density variability
 620 in the magnetosheath are stronger when IMF tends toward a radial direction. Similarly,
 621 using IAPIC, the dawn-dusk asymmetry in the magnetosheath and in the solar wind is
 622 investigated. In our work, the MP shape in Fig. 3, shows how asymmetric the dawn-dusk
 623 are. A result that is confirmed in Fig. 11, IMF, density, temperature and ion velocity are
 624 tested at the dusk-dawn flanks asymmetry in the magnetosheath. The magnetosheath, left
 625 to the vertical blue dashed line, all the parameters are asymmetric. This is consistent with
 626 (Turc et al., 2020). The vertical red dashed line shows the MP position at $-6R_E$ at the dusk
 627 flank at distance 8.5, 8.6 for radial and non-radial IMF. Whilst the vertical green dashed line
 628 shows the position at $+6R_E$ at the dawn flank. The solar wind parameters at the MP at
 629 subsolar point, dusk and dawn flanks are then quantified and tabulated in Table 5.

630 Finally, our analysis of the location, shape and size of the MP with the techniques
 631 developed for that purpose, in addition to the ability to quantify plasma parameters in 3D
 632 to track asymmetries in the dusk-dawn and south-north direction our code is applicable to
 633 planetary and exoplanetary magnetospheres. Furthermore, our findings can also contribute
 634 to alternative methods for a better analysis of soft x-ray imaging of the magnetosphere
 635 (Sibeck et al., 2018) in a complementary manner. This includes the MP, the cusp dynamics,
 636 the magnetosheath that is related to density structure which can be deduced from soft x-ray
 637 observation.

638 Most current support to the SMILE mission is based on MHD modeling (SMILE work-
 639 ing group). In light of the results obtained so far (see Figs. 2 and 3, and Tables 4), our

640 global 3D electromagnetic kinetic code is providing another point of view on the range of
 641 expected boundary locations under various solar wind flux. An accurate estimation of those
 642 boundary locations are key to interpret X-ray signal that will be detected by SXI, the SMILE
 643 X-ray detector. In addition, our simulations provide details about ions kinetic properties
 644 locally and on global scales (eg. Fig. 4), an additional tool for coupling plasma properties
 645 that will be detected by the light Ion Analyser (LIA) and large scale structure that will
 646 imaged by SXI. In light of the results obtained so far, we propose IAPIC, as a global 3D
 647 electromagnetic kinetic code to simulate the MP, the cusps, and the magnetosheath, which
 648 should enhance the science return of space missions like the CSA – ESA SMILE mission.

649 5 Summary and Conclusion

650 We have utilized a three-dimensional kinetic particle-in-cell code (IAPIC) to determine
 651 the size, shape and location of the Earth’s magnetopause with a dipole tilt of 31° in response
 652 to solar wind conditions of radial ($B=B_x$) and non-radial ($B_z < B_x, B_y$) IMF, covering
 653 the range of quasi-radial IMF that takes a cone angle between 0 and 50° . The simulations
 654 show the MP expanding anti-sunward and predict asymmetric magnetosphere in both IMF
 655 orientations.

656 Using a reference MP size ($10.3 R_E$) independently derived from (Shue et al., 1997),
 657 the findings of this study are summarized as follows:

- 658 1. The MP expands from 10.3 to $10.8R_E$ for the bulk flow and to $10.5R_E$ when effect of
 659 the backstreaming ions are dropped from calculations along OX axis for radial IMF.
 660 In other words, 40% of the observed expansion is due to backstreaming solar wind
 661 particles. Moreover, along tilted magnetic axis, the MP expansion is 10.3 to 11.9 and
 662 11.5 respectively.
- 663 2. For non radial IMF, the expansion is from 10.3 to 11.7 and to $11.3R_E$ for bulk flow
 664 and 10.3 to 12.0 and $11.6R_E$ when backstreaming ions are not accounted for in the
 665 flow.

- 666 3. The expansion rate for non radial IMF is 1.4 and $1.7R_E$ along OX and tilt axis
667 for bulk flow is comparable with the average expansion of 1.3-1.5 R_E reported from
668 Themis observations (Jelínek et al., 2010; Suvorova et al., 2010), without being forced
669 to modify the input solar wind parameters as done by MHD model (Samsonov et al.,
670 2017).
- 671 4. The expansion rate along tilted magnetic axes is larger for both IMF orientation
672 than OX plane. This result is explained by the presence of the current sheet that is
673 naturally predicted by our kinetic simulation in the magnetic equator. For reference,
674 the presence of the current sheet indicates that an additional plasma, entering from
675 the tail, will provide an additional pressure from inside (opposite to SW pressure)
676 that explains why our MP position is always larger along the tilt than the OX axis
677 in the XY plane.
- 678 5. The backstreaming ions contribution to the bulk flow is 16.5%, and 20% for radial
679 and non-radial IMF respectively along the OX axis in the dayside magnetosphere.
- 680 6. When deriving the MP position using the maximum density steepening method, the
681 backstreaming ions(characterized and quantified in this study) do not impact the
682 measured size of the MP for both IMF orientations along both OX and tilted axis.
- 683 7. In contrast, when the magnetopause is derived using pressure system balance, back-
684 streaming ions expand the magnetopause by 0.3 – 0.4 R_E (Table 4).
- 685 8. The difference between magnetopause derivation using maximum density steepening
686 (Garcia & Hughes, 2007; J. Lu et al., 2015) and the pressure systems balance using
687 definition of dynamic pressure as in (e.g., Willis, 1978, Eq. 3) is consistent with the
688 conclusion drawn by (Samsonov et al., 2020) that density and velocity act differently
689 as a component of dynamic pressure in the pressure system balance. In our study, we
690 also considered the effect of thermal pressure in the magnetosheath in the pressure
691 balance.
- 692 9. We present new results showing the magnetopause shape in spherical polar coordi-
693 nates for the two IMF directions. This new technique along with the magnetopause

694 derivations in Table 4 and Fig. 2 enables us to anticipate the sizes, shapes and loca-
 695 tions of magnetopause for all magnetized planets, including magnetized exoplanets.
 696 Additionally, this technique accounts for the backstreaming ion contribution to the
 697 data used to derive the magnetopause shape, a key information that is not available
 698 with other types of simulations.

699 10. The current study enabled us to derive the solar wind temperature anisotropy, thus
 700 paving a research road to study kinetic microinstabilities in the solar wind-magnetosphere
 701 coupling (see Figs. 8). For non-radial IMF, T_{\perp}/T_{\parallel} is large and equal ≈ 6 for ions and
 702 ≈ 1.6 for electrons. On the other hand, the T_{\perp}/T_{\parallel} for radial IMF equal to 1.8 and 2.2
 703 for ions and electrons respectively. The $T_{\perp e}/T_{\parallel e}$ ratio can be employed to predicts
 704 whistler waves like those observed by MMS((Le Contel et al., 2016)). Temperature
 705 anisotropy linked to magnetic reconcentration is widely discussed i.e. (Gingell et al.,
 706 2015),

707 11. The 3D velocity distribution function (Fig. 10) shows that backstreaming ions ap-
 708 pear upstream to distances of about $-20R_E$. Draping of the IMF, and temperature
 709 anisotropy in the magnetosheath, give rise to a complex structure that results in the
 710 asymmetry observed in the dawn-dusk and north-south directions. The dawn-dusk
 711 asymmetry is quantified in the current paper by tracking solar wind parameters at
 712 $\pm 6R_E$ cut parallel to OX plane. In Table 5, the solar wind parameters are measured
 713 at 10.8 and 11.7 R_E along the three parallel planes. Derived numbers at the MP
 714 position show the asymmetry numerically. In Fig. 11, the asymmetry is depicted for
 715 both IMF orientations as seen by the different color lines in each sub-figure.

716 12. In light of the results so far obtained, our findings are considered an additional and
 717 key modeling supports to future near-Earth exploration projects, in additions to outer
 718 planets moons and magnetospheres. For example, the newly developed technique to
 719 map the MP shape and position, or the ability to track backstreaming ions and
 720 their characterizations and their kinetic impact on the plasma flow will contribute

721 to deepen our understanding about the kinetic behavior of plasma in the solar wind
722 magnetosphere coupling and the study of exoplanets magnetospheres.

723 **Future Directions**

724 Radial and non-radial conditions are relatively infrequent configurations of the IMF at Earth,
725 but closer to the Sun, the Parker spiral becomes more and more radial. This suggests that
726 radial IMF conditions are more common at Mercury, which has recently been investigated
727 by MESSENGER and will soon be visited by the BepiColombo spacecraft. Furthermore,
728 Mercury's magnetosphere is much smaller as the magnetopause standoff position is only at
729 about $2R_M$ (R_M being the Mercury radius) and the ion gyroradius is about the size of the
730 planet. Finite Larmor radius effects are expected to play an ever more important role than
731 in the Earth's case (e.g., Johnson et al., 2014; Paral & Rankin, 2013). Mercury is therefore
732 a natural laboratory for investigating radial IMF and related kinetic effects and we will
733 prepare simulations in advance of BepiColombo's arrival at Mercury. Planets even closer to
734 their stars are common in the galaxy (NASA Exoplanets Archive *doi* = 10.26133/NEA2),
735 suggesting that, particularly around cooler M- and K-type stars, radial IMF may be a
736 common condition. This impacts the structure of their magnetospheres and may influence
737 the escape of planetary atmospheric and ionospheric constituents over time. The kinetic
738 aspect of our approach is particularly sensitive to the dynamics of the bow shock, which
739 may be highly variable in the neighborhood of a small star (Cohen et al., 2015), potentially
740 producing accelerated particles and observable radio emissions (Cohen et al., 2018). One
741 more issue that will be considered for near future work is the impact of the magnetosphere-
742 ionosphere-magnetosheath coupling on magnetopause location. We have tracked in the
743 past H^+ and O^+ ions outflow from the ionospheric origin in the dayside magnetosphere
744 (S. M. Baraka & Ben-Jaffel, 2015). IAPIC can also be used to study outflow of plasmasphere
745 low energy ions.

746 **Acknowledgments**

747 This work is carried out using binary data generated by IAPIC, a pic code that is a mod-
748 ified version of the Tristan code that is available to the public through GitHub: [https://](https://github.com/ntoles/tristan-mp-pitp)
749 github.com/ntoles/tristan-mp-pitp. THEMIS, ACE, and, Wind data are available at

750 <http://amda.cdpp.eu/>. The used data for generating results is available at ([https://doi](https://doi.org/10.48392/bar-001)
751 [.org/10.48392/bar-001](https://doi.org/10.48392/bar-001)). S Baraka acknowledges the NIA NASA grant # NNX15AE05G
752 for supporting this research via the Living and Breathing Planet project. L. Ben-Jaffel
753 acknowledges support from CNES under project PACES. S. Baraka thanks IAP-CNRS for
754 using their computing resources facilities and generating the simulation data. Also S Baraka
755 thanks Daniel Pomarede from Atomic Energy Commission, CNRS, France for providing SD-
756 vision software .

757 References

- 758 Akasofu, S.-I. (1991). Development of magnetospheric physics. *Magnetospheric Substorms*,
759 *64*, 3–9.
- 760 Akasofu, S.-I., Roederer, M., & Krimigis, S. (1982). Dawn-dusk asymmetry of the tail region
761 of the magnetosphere of saturn and the interplanetary magnetic field. *Planetary and*
762 *Space Science*, *30*(10), 1061–1063.
- 763 Artemyev, A., & Zelenyi, L. (2012, December). Kinetic Structure of Current Sheets in
764 the Earth Magnetotail. *Space Science Reviews*, *178*(2-4), 419–440. doi: 10.1007/
765 s11214-012-9954-5
- 766 Asbridge, J., Bame, S., & Strong, I. (1968). Outward flow of protons from the earth’s bow
767 shock. *Journal of Geophysical Research*, *73*(17), 5777–5782.
- 768 Baraka, S. (2016, April). Large Scale Earth’s Bow Shock with Northern IMF as Simulated
769 by PIC Code in Parallel with MHD Model. *Journal of Astrophysics and Astronomy*,
770 *37*(2), 1–16. doi: 10.1007/s12036-016-9389-6
- 771 Baraka, S., & Ben-Jaffel, L. (2007, June). Sensitivity of the Earth’s magnetosphere to
772 solar wind activity: Three-dimensional macroparticle model. *Journal of Geophysical*
773 *Research (Space Physics)*, *112*, 6212. doi: 10.1029/2006JA011946
- 774 Baraka, S., & Ben-Jaffel, L. (2011). Impact of solar wind depression on the dayside
775 magnetosphere under northward interplanetary magnetic field. *Annales Geophysicae*,
776 *29*(1), 31–46. Retrieved from <https://www.ann-geophys.net/29/31/2011/> doi:
777 10.5194/angeo-29-31-2011
- 778 Baraka, S. M., & Ben-Jaffel, L. (2015). Magnetospheric dynamical and morphological
779 response to multi-species plasma supply from the ionosphere: New comprehensive 3d
780 pic simulation. *AGUFM*, *2015*, SM23B–2552.
- 781 Ben-Jaffel, L., & Ballester, G. (2013, May). Hubble Space Telescope detection of oxygen in
782 the atmosphere of exoplanet HD 189733b. *Astronomy & Astrophysics*, *553*, A52. doi:
783 10.1051/0004-6361/201221014
- 784 Ben-Jaffel, L., & Ballester, G. E. (2014, April). Transit of Exomoon Plasma Tori: New
785 Diagnosis. *apjl*, *785*, L30. doi: 10.1088/2041-8205/785/2/L30
- 786 Berchem, J., Richard, R. L., Escoubet, C. P., Wing, S., & Pitout, F. (2016, January). Asym-
787 metrical response of dayside ion precipitation to a large rotation of the imf. *Journal*
788 *of Geophysical Research (Space Physics)*, *121*, 263–273. Retrieved from [https://](https://ui.adsabs.harvard.edu/abs/2016JGRA..121..263B)
789 ui.adsabs.harvard.edu/abs/2016JGRA..121..263B doi: 10.1002/2015JA021969
- 790 Blanco-Cano, X., Omid, N., & Russell, C. (2006). Macrostructure of collisionless bow
791 shocks: 2. ULF waves in the foreshock and magnetosheath. *Journal of Geophysical*
792 *Research: Space Physics (1978–2012)*, *111*(A10).
- 793 Blanco-Cano, X., Omid, N., & Russell, C. (2009). Global hybrid simulations: Foreshock
794 waves and cavitons under radial interplanetary magnetic field geometry. *Journal of*
795 *Geophysical Research: Space Physics*, *114*(A1).
- 796 Bobra, M., Petrincic, S., Fuselier, S., Claffin, E., & Spence, H. E. (2004). On the solar wind
797 control of cusp aurora during northward imf. *Geophysical research letters*, *31*(4).
- 798 Bonifazi, C., & Moreno, G. (1981a). Reflected and diffuse ions backstreaming from the
799 earth’s bow shock 1. basic properties. *Journal of Geophysical Research: Space Physics*,
800 *86*, 4397–4404. doi: 10.1029/ja086ia06p04397
- 801 Bonifazi, C., & Moreno, G. (1981b). Reflected and diffuse ions backstreaming from the
802 Earth’s bow shock 2. Origin. *Journal of Geophysical Research: Space Physics (1978–*

- 803 2012), 86(A6), 4405–4413.
- 804 Bonifazi, C., Moreno, G., Lazarus, A. J., & Sullivan, J. D. (1980, November). Deceleration
805 of the solar wind in the earth’s foreshock region - ISEE 2 and IMP 8 observations.
806 *Journal of Geophysical Research*, 85, 6031–6038. doi: 10.1029/JA085iA11p06031
- 807 Brackbill, J. U. (2011). A comparison of fluid and kinetic models of steady magnetic recon-
808 nection. *Physics of Plasmas (1994-present)*, 18(3), 032309. doi: 10.1063/1.3568828
- 809 Buneman, O., Neubert, T., & Nishikawa, K.-I. (1992). Solar wind-magnetosphere interaction
810 as simulated by a 3-d em particle code. *IEEE transactions on plasma science*, 20(6),
811 810–816.
- 812 Cai, D., Esmaeili, A., Lembège, B., & Nishikawa, K.-I. (2015). Cusp dynamics under
813 northward imf using three-dimensional global particle-in-cell simulations. *Journal of*
814 *Geophysical Research: Space Physics*, 120(10), 8368–8386.
- 815 Cai, D., Li, Y., Nishikawa, K.-I., Xiao, C., Yan, X., & Pu, Z. (2003). Parallel 3-D Elec-
816 tromagnetic Particle Code Using High Performance FORTRAN: Parallel TRISTAN.
817 In *Space Plasma Simulation* (Vol. 615, pp. 25–53). Springer Berlin Heidelberg. doi:
818 10.1007/3-540-36530-3_2
- 819 Cohen, O., Ma, Y., Drake, J. J., Glocer, A., Garraffo, C., Bell, J. M., & Gombosi, T. I.
820 (2015, jun). THE INTERACTION OF VENUS-LIKE, m-DWARF PLANETS WITH
821 THE STELLAR WIND OF THEIR HOST STAR. *The Astrophysical Journal*, 806(1),
822 41. Retrieved from [https://doi.org/10.1088/](https://doi.org/10.1088/0004-637x/806/1/41)
823 [0004-637x/806/1/41](https://doi.org/10.1088/0004-637x/806/1/41) doi: 10.1088/
824 0004-637x/806/1/41
- 825 Cohen, O., Moschou, S.-P., Glocer, A., Sokolov, I. V., Mazeh, T., Drake, J. J., ... Alvarado-
826 Gómez, J. D. (2018, oct). Exoplanet modulation of stellar coronal radio emission.
827 *The Astronomical Journal*, 156(5), 202. Retrieved from [https://doi.org/10.3847/](https://doi.org/10.3847/1538-3881/aae1f2)
828 [1538-3881/aae1f2](https://doi.org/10.3847/1538-3881/aae1f2) doi: 10.3847/1538-3881/aae1f2
- 829 Dimmock, A., Nykyri, K., Osmane, A., Karimabadi, H., & Pulkkinen, T. (2017). Dawn-
830 dusk asymmetries of the earth’s dayside magnetosheath in the magnetosheath inter-
831 planetary medium reference frame. *Dawn-Dusk Asymmetries in Planetary Plasma*
832 *Environments*, 49–72.
- 833 Dimmock, A. P., Nykyri, K., Karimabadi, H., Osmane, A., & Pulkkinen, T. I. (2015, April).
834 A statistical study into the spatial distribution and dawn-dusk asymmetry of dayside
835 magnetosheath ion temperatures as a function of upstream solar wind conditions.
836 *Journal of Geophysical Research (Space Physics)*, 120(4), 2767-2782. doi: 10.1002/
837 2014JA020734
- 838 Dimmock, A. P., Nykyri, K., & Pulkkinen, T. I. (2014, August). A statistical study of
839 magnetic field fluctuations in the dayside magnetosheath and their dependence on
840 upstream solar wind conditions. *Journal of Geophysical Research (Space Physics)*,
841 119(8), 6231-6248. doi: 10.1002/2014JA020009
- 842 Dušík, Š., Granko, G., Šafránková, J., Němeček, Z., & Jelínek, K. (2010). Imf cone angle
843 control of the magnetopause location: Statistical study. *Geophysical Research Letters*,
844 37(19).
- 845 Eastwood, J. P. (2008). The science of space weather. *Philosophical Transactions of the*
846 *Royal Society A: Mathematical, Physical and Engineering Sciences*, 366(1884), 4489–
847 4500.
- 848 Fairfield, D., Baumjohann, W., Paschmann, G., Lühr, H., & Sibeck, D. (1990). Upstream
849 pressure variations associated with the bow shock and their effects on the magneto-
850 sphere. *Journal of Geophysical Research: Space Physics*, 95(A4), 3773–3786.
- 851 Garcia, K., & Hughes, W. (2007). Finding the lyon-fedder-mobarry magnetopause: A
852 statistical perspective. *Journal of Geophysical Research: Space Physics*, 112(A6).
- 853 Gingell, P. W., Burgess, D., & Matteini, L. (2015, March). The Three-dimensional Evolution
854 of Ion-scale Current Sheets: Tearing and Drift-kink Instabilities in the Presence of
855 Proton Temperature Anisotropy. *The Astrophysical Journal*, 802(1), 4. doi: 10.1088/
856 0004-637X/802/1/4
- 857 Greenstadt, E. W., Green, I. M., Inouye, G. T., Hundhausen, A. J., Bame, S. J., & Strong,
I. B. (1968, January). Correlated magnetic field and plasma observations of the Earth’s

- 858 bow shock. *textbackslashjgr*, 73, 51. doi: 10.1029/JA073i001p00051
- 859 Grygorov, K., Šafránková, J., Němeček, Z., Pi, G., Přeč, L., & Urbář, J. (2017). Shape
860 of the equatorial magnetopause affected by the radial interplanetary magnetic field.
861 *Planetary and Space Science*, 148, 28–34.
- 862 Haaland, S., Lybekk, B., Maes, L., Laundal, K., Pedersen, A., Tenfjord, P., ... Snekvik,
863 K. (2017). North-south asymmetries in cold plasma density in the magnetotail lobes:
864 Cluster observations. *Journal of Geophysical Research: Space Physics*, 122(1), 136–
865 149.
- 866 Haaland, S., Reistad, J., Tenfjord, P., Gjerloev, J., Maes, L., DeKeyser, J., ... Dorville, N.
867 (2014). Characteristics of the flank magnetopause: Cluster observations. *Journal of*
868 *Geophysical Research: Space Physics*, 119(11), 9019–9037.
- 869 Haaland, S., Runov, A., Artemyev, A., & Angelopoulos, V. (2019). Characteristics of the
870 flank magnetopause: Themis observations. *Journal of Geophysical Research: Space*
871 *Physics*, 124(5), 3421–3435.
- 872 Heikkilä, W. J. (2011). *Earth's Magnetosphere: Formed by the Low-latitude Boundary*
873 *Layer*. Elsevier.
- 874 Jacobsen, K. S., Phan, T. D., Eastwood, J. P., Sibeck, D. G., Moen, J. I., Angelopoulos, V.,
875 ... Fornaçon, K.-H. (2009). THEMIS observations of extreme magnetopause motion
876 caused by a hot flow anomaly. *Journal of Geophysical Research (Space Physics)*, 114,
877 8210. Retrieved from <http://adsabs.harvard.edu/abs/2009JGRA...114.8210J>
- 878 Jelínek, K., Němeček, Z., Šafránková, J., Shue, J.-H., Suvorova, A. V., & Sibeck, D. G.
879 (2010). Thin magnetosheath as a consequence of the magnetopause deformation:
880 THEMIS observations. *Journal of Geophysical Research (Space Physics)*, 115, 10203.
881 Retrieved from <http://adsabs.harvard.edu/abs/2010JGRA...11510203J>
- 882 Johnson, J. R., Wing, S., & Delamere, P. A. (2014). Kelvin helmholtz instability in planetary
883 magnetospheres. *Space Science Reviews*, 184(1-4), 1–31.
- 884 Karimabadi, H., Krauss-Varban, D., Huba, J., & Vu, H. (2004). On magnetic reconnection
885 regimes and associated three-dimensional asymmetries: Hybrid, hall-less hybrid, and
886 hall-mhd simulations. *Journal of Geophysical Research: Space Physics*, 109(A9).
- 887 Karimabadi, H., Roytershteyn, V., Vu, H. X., Omelchenko, Y. A., Scudder, J., Daughton,
888 W., ... Geveci, B. (2014). The link between shocks, turbulence, and magnetic reconnection
889 in collisionless plasmas. *Physics of Plasmas*, 21, 062308. doi: 10.1063/1.4882875
- 890 Lavraud, B., Borovsky, J. E., Génot, V., Schwartz, S. J., Birn, J., Fazakerley, A. N., ...
891 Wild, J. A. (2009). Tracing solar wind plasma entry into the magnetosphere using
892 ion-to-electron temperature ratio. *Geophys. Res. Lett.*, 36, 18109. Retrieved from
893 <http://adsabs.harvard.edu/abs/2009GeoRL...3618109L>
- 894 Le Contel, O., Retinò, A., Breuillard, H., Mirioni, L., Robert, P., Chasapis, A., ... Saito,
895 Y. (2016, June). Whistler mode waves and Hall fields detected by MMS during a
896 dayside magnetopause crossing. *Geophysical Research Letters*, 43(12), 5943–5952. doi:
897 10.1002/2016GL068968
- 898 Lindman, E. (1975). “Free-space” boundary conditions for the time dependent wave equation.
899 *J. Comput. Phys.*, 18(1), 66–78.
- 900 Liu, Y.-H., Li, T., Hesse, M., Sun, W., Liu, J., Burch, J., ... Huang, K. (2019). Three-
901 dimensional magnetic reconnection with a spatially confined x-line extent: Implica-
902 tions for dipolarizing flux bundles and the dawn-dusk asymmetry. *Journal of Geo-*
903 *physical Research: Space Physics*, 124(4), 2819–2830.
- 904 Lu, J., Wang, M., Kabin, K., Zhao, J., Liu, Z.-Q., Zhao, M., & Li, G. (2015). Pressure
905 balance across the magnetopause: Global mhd results. *Planetary and Space Science*,
906 106, 108–115.
- 907 Lu, S., Lin, Y., Angelopoulos, V., Artemyev, A., Pritchett, P., Lu, Q., & Wang, X. (2016).
908 Hall effect control of magnetotail dawn-dusk asymmetry: A three-dimensional global
909 hybrid simulation. *Journal of Geophysical Research: Space Physics*, 121(12), 11–882.
- 910 Luo, H., Chen, G., Du, A., & Xu, W. (2013). Solar wind dependence of energy coupling
911 between solar wind and magnetosphere during intense northward imfs. *Planetary and*
912 *Space Science*, 79, 82–89.

- 913 Masters, A., Slavin, J., DiBraccio, G., Sundberg, T., Winslow, R., Johnson, C., ... Korth,
914 H. (2013). A comparison of magnetic overshoots at the bow shocks of mercury and
915 saturn. *Journal of Geophysical Research: Space Physics*, *118*(7), 4381–4390.
- 916 Merka, J., Szabo, A., Šafránková, J., & Němeček, Z. (2003). Earth’s bow shock and
917 magnetopause in the case of a field-aligned upstream flow: Observation and model
918 comparison. *Journal of Geophysical Research: Space Physics (1978–2012)*, *108*(A7),
919 –.
- 920 Němeček, Z., Šafránková, J., Zastenker, G. N., Pišoft, P., & Jelínek, K. (2002, April).
921 Low-frequency variations of the ion flux in the magnetosheath. *Planetary and Space
922 Science*, *50*(5-6), 567-575. doi: 10.1016/S0032-0633(02)00036-3
- 923 Omid, N., Blanco-Cano, X., Russell, C. T., & Karimabadi, H. (2004, January). Dipolar
924 magnetospheres and their characterization as a function of magnetic moment. *Ad-
925 vances in Space Research*, *33*, 1996–2003. doi: 10.1016/j.asr.2003.08.041
- 926 Palmroth, M., Ganse, U., Pfau-Kempf, Y., Battarbee, M., Turc, L., Brito, T., ... von Althaus,
927 S. (2018, August). Vlasov methods in space physics and astrophysics. *Living Reviews
928 in Computational Astrophysics*, *4*(1), 1. doi: 10.1007/s41115-018-0003-2
- 929 Paral, J., & Rankin, R. (2013). Dawn–dusk asymmetry in the kelvin–helmholtz instability
930 at mercury. *Nature Communications*, *4*(1), 1–5.
- 931 Park, J.-S., Shue, J.-H., Kim, K.-H., Pi, G., Němeček, Z., & Šafránková, J. (2016, July).
932 Global expansion of the dayside magnetopause for long-duration radial IMF events:
933 Statistical study on GOES observations. *Journal of Geophysical Research (Space
934 Physics)*, *121*(7), 6480–6492. doi: 10.1002/2016JA022772
- 935 Parks, G. K. (1991). Physics of space plasmas—an introduction. *Redwood City, CA, Addison-
936 Wesley Publishing Co., 1991, 547 p.*
- 937 Paschmann, G., Baumjohann, W., Scokopke, N., Phan, T. D., & Luehr, H. (1993, August).
938 Structure of the dayside magnetopause for low magnetic shear. *Journal of Geophysical
939 Research(Space Physics)*, *98*(A8), 13409-13422. doi: 10.1029/93JA00646
- 940 Paularena, K., Richardson, J., Kolpak, M., Jackson, C., & Siscoe, G. (2001). A dawn-dusk
941 density asymmetry in earth’s magnetosheath. *Journal of Geophysical Research: Space
942 Physics*, *106*(A11), 25377–25394.
- 943 Phan, T. D., Paschmann, G., Baumjohann, W., Scokopke, N., & Luehr, H. (1994, January).
944 The magnetosheath region adjacent to the dayside magnetopause: AMPTE/IRM ob-
945 servations. *Journal of Geophysical Research (Space Physics)*, *99*(A1), 121-142. doi:
946 10.1029/93JA02444
- 947 Pi, G., Němeček, Z., Šafránková, J., Grygorov, K., & Shue, J.-H. (2018). Formation of
948 the dayside magnetopause and its boundary layers under the radial imf. *Journal of
949 Geophysical Research: Space Physics*, *123*(5), 3533–3547.
- 950 Samsonov, A. (2006, January). Numerical modelling of the Earth’s magnetosheath for
951 different IMF orientations. *Advances in Space Research*, *38*(8), 1652-1656. doi: 10
952 .1016/j.asr.2005.06.009
- 953 Samsonov, A. A. (2011, January). Propagation of inclined interplanetary shock through
954 the magnetosheath. *Journal of Atmospheric and Solar-Terrestrial Physics*, *73*, 30–39.
955 doi: 10.1016/j.jastp.2009.10.014
- 956 Samsonov, A. A., Bogdanova, Y. V., Branduardi-Raymont, G., Sibeck, D. G., & Toth, G.
957 (2020). Is the Relation Between the Solar Wind Dynamic Pressure and the Mag-
958 netopause Standoff Distance so Straightforward? *Geophys. Res. Lett.*, *47*(8). doi:
959 10.1029/2019GL086474
- 960 Samsonov, A. A., Němeček, Z., Šafránková, J., & Jelínek, K. (2012, May). Why does the
961 subsolar magnetopause move sunward for radial interplanetary magnetic field? *Jour-
962 nal of Geophysical Research (Space Physics)*, *117*, 5221. doi: 10.1029/2011JA017429
- 963 Samsonov, A. A., Sibeck, D. G., Šafránková, J., Němeček, Z., & Shue, J. H. (2017,
964 March). A method to predict magnetopause expansion in radial IMF events by MHD
965 simulations. *Journal of Geophysical Research (Space Physics)*, *122*(3), 3110-3126. doi:
966 10.1002/2016JA023301
- 967 Shue, J. H., Chao, J. K., Fu, H. C., Russell, C. T., Song, P., Khurana, K. K., & Singer,

- 968 H. J. (1997, May). A new functional form to study the solar wind control of the mag-
 969 netopause size and shape. *Journal of Geophysical Research (Space Physics)*, *102*(A5),
 970 9497-9512. doi: 10.1029/97JA00196
- 971 Shue, J.-H., Chao, J.-K., Song, P., McFadden, J., Suvorova, A., Angelopoulos, V., ...
 972 Plaschke, F. (2009). Anomalous magnetosheath flows and distorted subsolar mag-
 973 netopause for radial interplanetary magnetic fields. *Geophysical Research Letters*,
 974 *36*(18).
- 975 Sibeck, D. G., Allen, R., Aryan, H., Bodewits, D., Brandt, P., Branduardi-Raymont, G., ...
 976 others (2018). Imaging plasma density structures in the soft x-rays generated by solar
 977 wind charge exchange with neutrals. *Space Science Reviews*, *214*(4), 79.
- 978 Sibeck, D. G., Decker, R. B., Mitchell, D. G., Lazarus, A. J., Lepping, R. P., & Szabo,
 979 A. (2001). Solar wind preconditioning in the flank foreshock: IMP 8 observations.
 980 *J. Geophys. Res.*, *106*, 21675–21688. Retrieved from [http://adsabs.harvard.edu/
 981 abs/2001JGR...10621675S](http://adsabs.harvard.edu/abs/2001JGR...10621675S)
- 982 Sorathia, K., Merkin, V., Ukhorskiy, A., Allen, R., Nykyri, K., & Wing, S. (2019). Solar
 983 wind ion entry into the magnetosphere during northward imf. *Journal of Geophysical
 984 Research: Space Physics*, *124*(7), 5461–5481.
- 985 Spreiter, J. R., & Alksne, A. Y. (1969). Plasma flow around the magnetosphere. *Reviews
 986 of Geophysics*, *7*(1-2), 11–50.
- 987 Suvorova, A., & Dmitriev, A. (2015). Magnetopause inflation under radial imf: Comparison
 988 of models. *Earth and Space Science*, *2*(4), 107–114.
- 989 Suvorova, A. V., Shue, J. H., Dmitriev, A. V., Sibeck, D. G., McFadden, J. P., Hasegawa,
 990 H., ... Němeček, Z. (2010, October). Magnetopause expansions for quasi-radial inter-
 991 planetary magnetic field: THEMIS and Geotail observations. *Journal of Geophysical
 992 Research (Space Physics)*, *115*(A10), A10216. doi: 10.1029/2010JA015404
- 993 Tan, B., Lin, Y., Perez, J., & Wang, X. (2011). Global-scale hybrid simulation of dayside
 994 magnetic reconnection under southward imf: Structure and evolution of reconnection.
 995 *Journal of Geophysical Research: Space Physics*, *116*(A2).
- 996 Treumann, R. A., & Baumjohann, W. (2013, December). Collisionless Magnetic Reconnec-
 997 tion in Space Plasmas. , *1*, 31. (arXiv: 1401.5995) doi: 10.3389/fphy.2013.00031
- 998 Turc, L., Tarvus, V., Dimmock, A., Battarbee, M., Ganse, U., Johlander, A., ... Palm-
 999 roth, M. (2020). Asymmetries in the earth’s dayside magnetosheath: results
 1000 from global hybrid-vlasov simulations. *Annales Geophysicae Discussions*, *2020*, 1–
 1001 24. Retrieved from <https://www.ann-geophys-discuss.net/angeo-2020-13/> doi:
 1002 10.5194/angeo-2020-13
- 1003 Turner, D., Wilson, L., Liu, T., Cohen, I., Schwartz, S., Osmane, A., ... others (2018).
 1004 Autogenous and efficient acceleration of energetic ions upstream of earth’s bow shock.
 1005 *Nature*, *561*(7722), 206–210.
- 1006 Villasenor, J., & Buneman, O. (1992). Rigorous charge conservation for local electromag-
 1007 netic field solvers. *Comput. Phys. Commun.*, *69*(2), 306–316.
- 1008 Šafránková, J., Němeček, Z., Santolík, O., Sibeck, D. G., Zastenker, G. N., & Skalsky, A.
 1009 (2000). The Flank Magnetopause: Interball Observations. *Advances in Space Research*,
 1010 *25*, 1503–1510. Retrieved from [http://adsabs.harvard.edu/abs/2000AdSpR...25
 1011 .1503S](http://adsabs.harvard.edu/abs/2000AdSpR...25)
- 1012 Walsh, A. P., Haaland, S., Forsyth, C., Keese, A. M., Kissinger, J., Li, K., ... Taylor,
 1013 M. G. G. T. (2014, July). Dawn-dusk asymmetries in the coupled solar wind-
 1014 magnetosphere-ionosphere system: a review. *Annales Geophysicae*, *32*, 705–737.
 1015 Retrieved from <https://ui.adsabs.harvard.edu/abs/2014AnGeo...32...705W> doi:
 1016 10.5194/angeo-32-705-2014
- 1017 Walsh, B. M. (2017). Magnetopause plasma parameters and asymmetries in solar wind-
 1018 magnetosphere coupling. *Dawn-Dusk Asymmetries in Planetary Plasma Environ-
 1019 ments*, 29–39.
- 1020 Walsh, B. M., Sibeck, D. G., Wang, Y., & Fairfield, D. H. (2012). Dawn-dusk asymmetries
 1021 in the Earth’s magnetosheath. *Journal of Geophysical Research (Space Physics)*, *117*,
 1022 12211. Retrieved from <http://adsabs.harvard.edu/abs/2012JGRA...11712211W>

- 1023 Wang, C.-P., Gkioulidou, M., Lyons, L. R., & Angelopoulos, V. (2012). Spatial distributions
1024 of the ion to electron temperature ratio in the magnetosheath and plasma sheet.
1025 *Journal of Geophysical Research: Space Physics*, *117*(A8).
- 1026 Wang, C.-P., Lyons, L. R., Weygand, J. M., Nagai, T., & McEntire, R. W. (2006). Equa-
1027 torial distributions of the plasma sheet ions, their electric and magnetic drifts, and
1028 magnetic fields under different interplanetary magnetic field b_z conditions. *Journal of*
1029 *Geophysical Research: Space Physics*, *111*(A4).
- 1030 Wang, J., Guo, Z., Ge, Y. S., Du, A., Huang, C., & Qin, P. (2018, October). The responses
1031 of the earth's magnetopause and bow shock to the IMF B_z and the solar wind dynamic
1032 pressure: a parametric study using the AMR-CESE-MHD model. *Journal of Space*
1033 *Weather and Space Climate*, *8*, A41. doi: 10.1051/swsc/2018030
- 1034 Willis, D. (1978). The magnetopause: Microstructure and interaction with magnetospheric
1035 plasma. *Journal of Atmospheric and Terrestrial Physics*, *40*(3), 301–322.
- 1036 Wing, S., Johnson, J. R., Chaston, C. C., Echim, M., Escoubet, C. P., Lavraud, B., ...
1037 Wang, C. P. (2014, November). Review of Solar Wind Entry into and Transport
1038 Within the Plasma Sheet. *Space Science Reviews*, *184*(1-4), 33-86. doi: 10.1007/
1039 s11214-014-0108-9
- 1040 Yu, Y., & Ridley, A. J. (2009, December). The response of the magnetosphere-ionosphere
1041 system to a sudden dynamic pressure enhancement under southward IMF conditions.
1042 *Annales Geophysicae*, *27*(12), 4391-4407. doi: 10.5194/angeo-27-4391-2009
- 1043 Zhang, H., Fu, S., Pu, Z., Lu, J., Zhong, J., Zhu, C., ... Liu, L. (2019, aug). Statis-
1044 tics on the magnetosheath properties related to magnetopause magnetic reconnec-
1045 tion. *The Astrophysical Journal*, *880*(2), 122. Retrieved from [https://doi.org/](https://doi.org/10.3847/1538-4357/ab290e)
1046 [10.3847/1538-4357/ab290e](https://doi.org/10.3847/1538-4357/ab290e) doi: 10.3847/1538-4357/ab290e

6 Figures

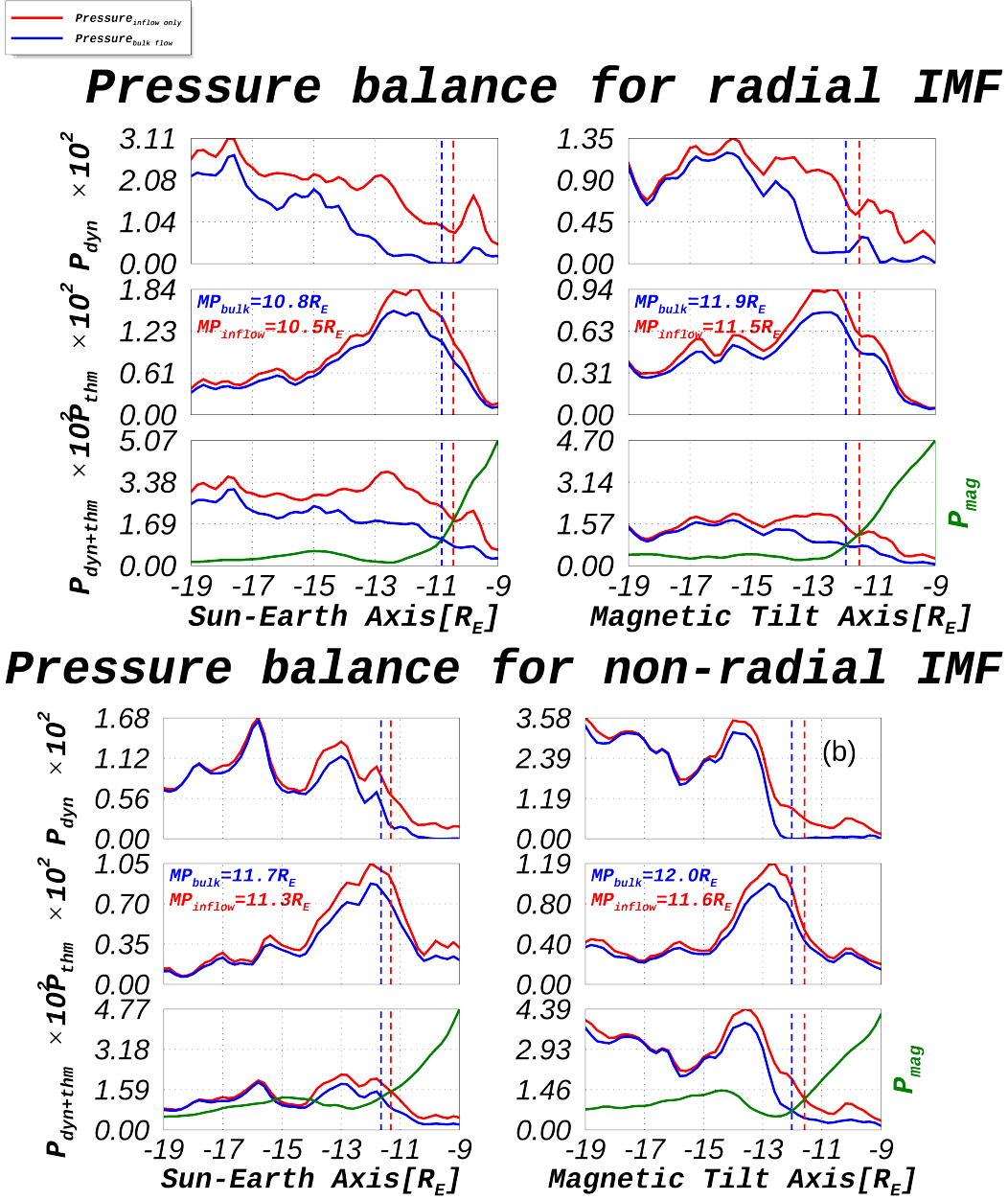


Figure 2. MP size derivation from pressure balance system measured radially at two locations. The MP is derived along the Earth-Sun axis(OX) and along magnetic equator axis (Tilt). Bulk flow(blue) and diffuse population(red) are shown for two IMF orientations(upper for radial and lower for non-radial). The backstreaming ions are not only seen at the bow shock, but everywhere in the simulation box

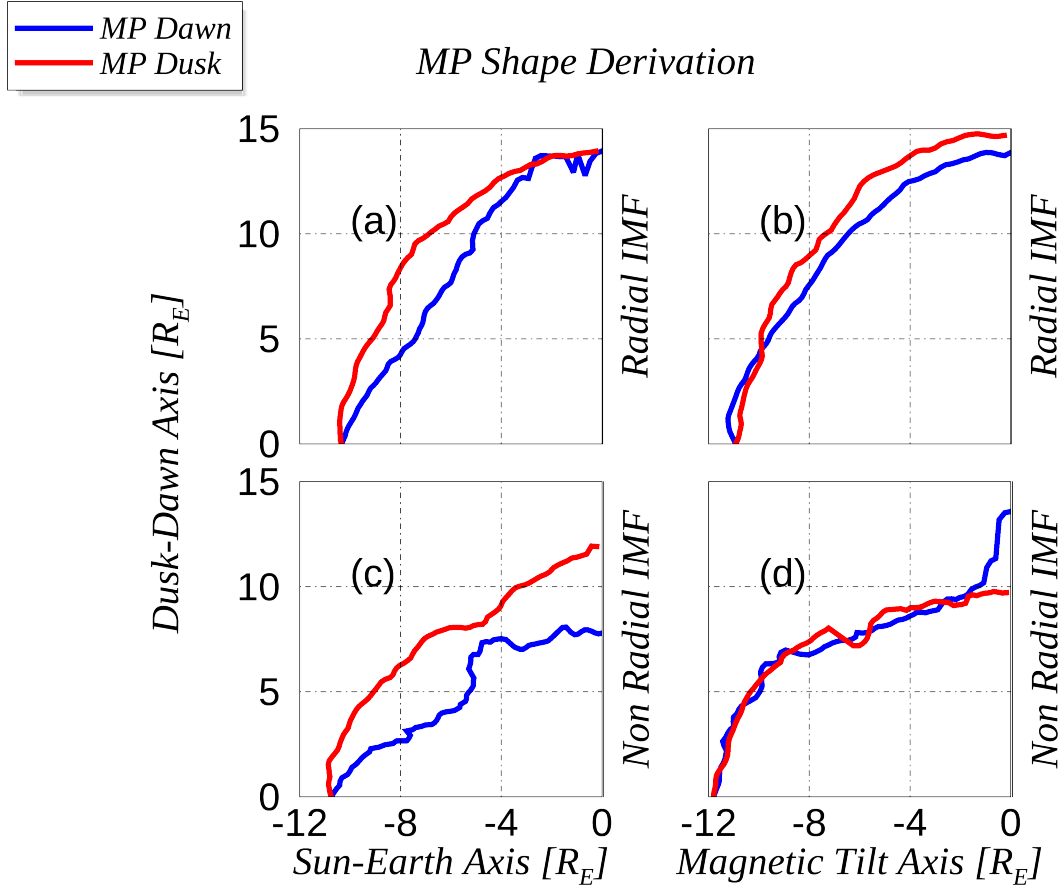


Figure 3. Panels (a) and (b) is the MP shape for radial IMF along Sun-Earth and Magnetic Tilted Axis, similarly panels (c) and (d) are the same for non-radial IMF. This Figure is aimed to show the shape of the MP, though the size shown here is approximately equivalent to the MP sizes derived from the density steepening.

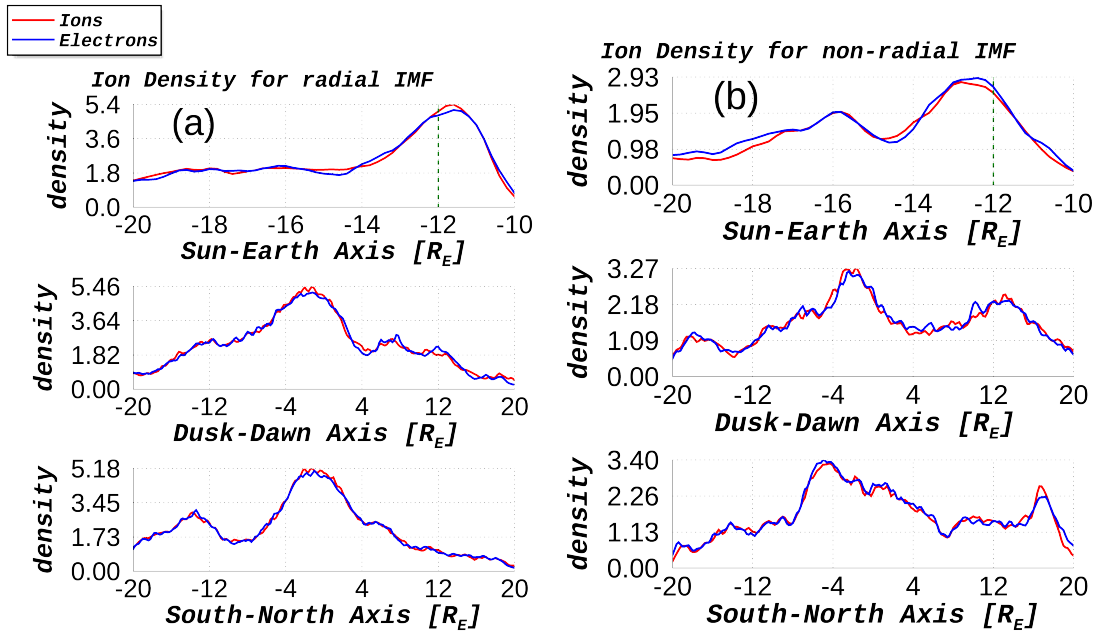


Figure 4. Ion and electron densities are plotted in 3D, along OX($Y=Z=0$), OY($X=12$, and $Z=0$), and OZ($X=12$, and $Y=0$), just outside the MP for radial IMF in panel A and for non-radial IMF in panel B. Their values are normalized to the initial densities. The density profile is plotted only in the dayside magnetosphere. This figure also shows the plasma quasi neutrality.

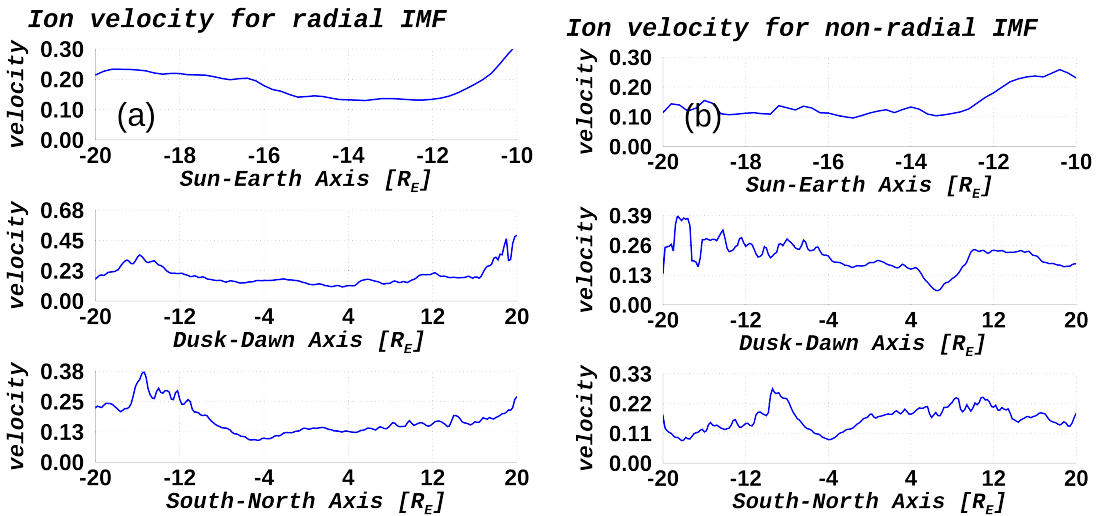


Figure 5. Ion velocity modulus for both IMF orientation are plotted in 3D as in Fig. 4.

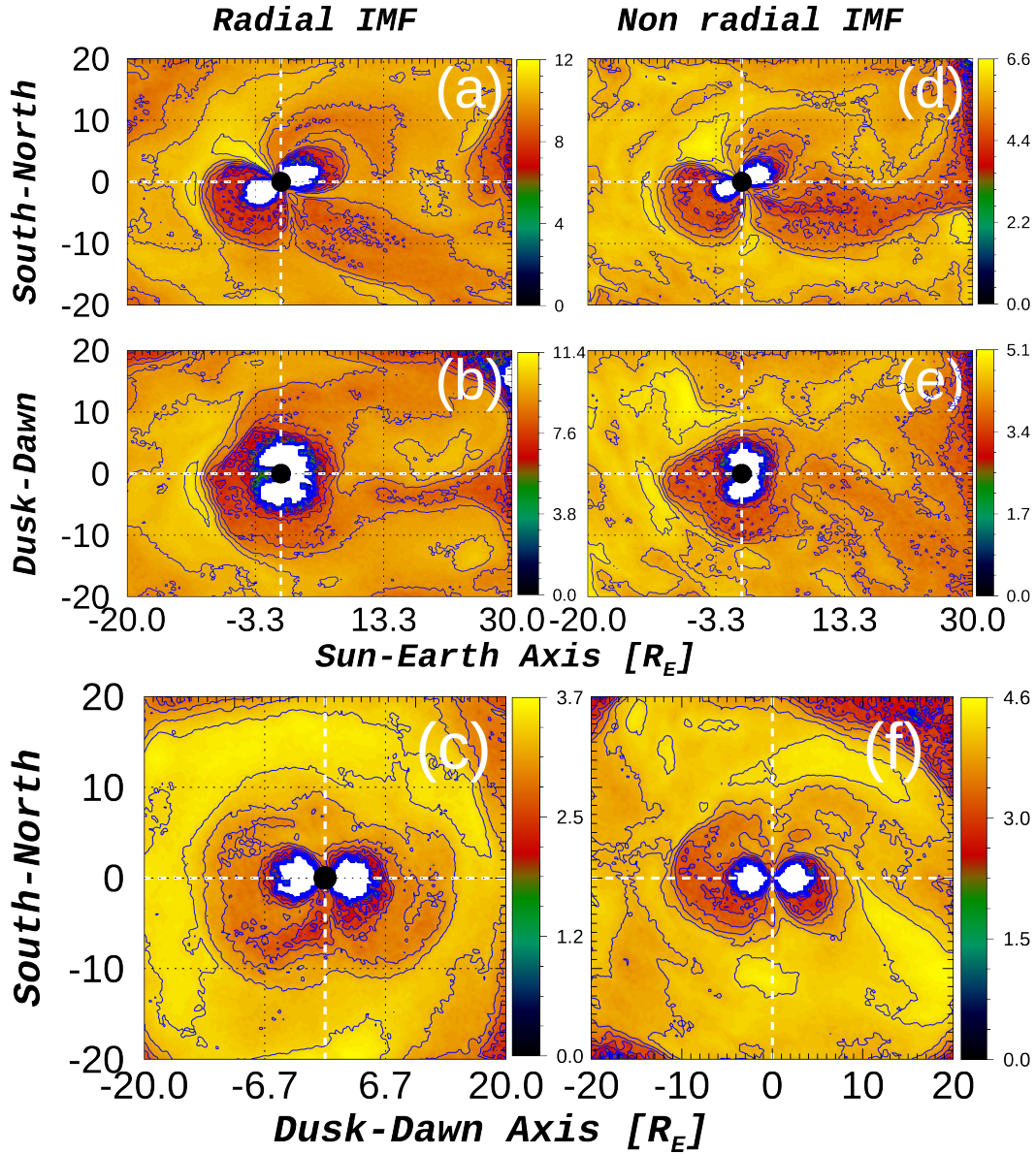


Figure 6. Fields topology in 3D for both IMF orientations. XZ and XY planes are taken in the dayside magnetosphere. YZ plane is plotted at around $12R_E$ outside the MP. Panels (a), (b), and (c) are for radial IMF and panels (d), (e), and (f) are for non radial IMF

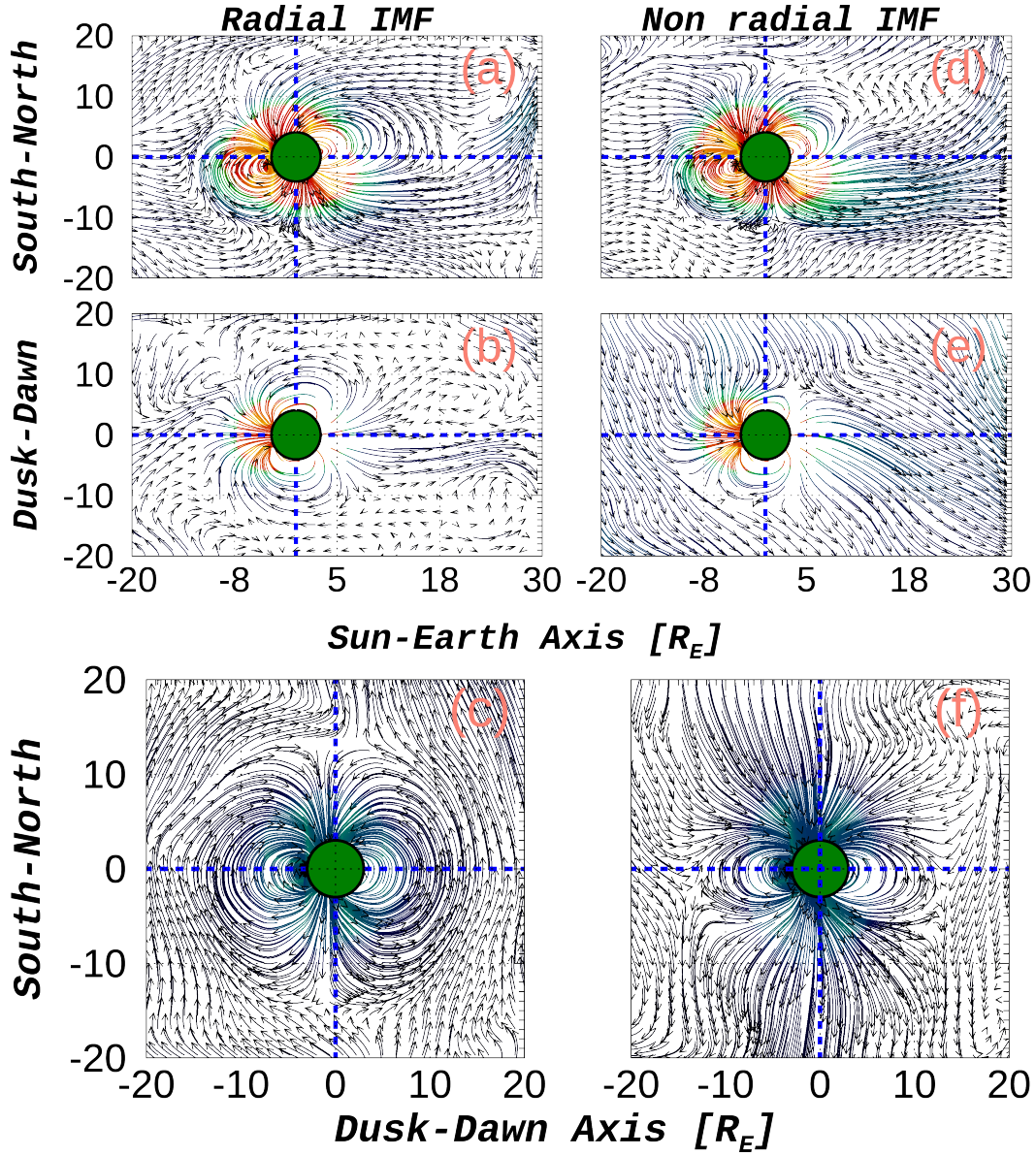


Figure 7. Solar wind density contour in 3D for both IMF orientations. XZ and XY planes are taken in the dayside magnetosphere. YZ contour is plotted at around $12R_E$ outside the MP. Panels (a), (b), and (c) are for radial IMF and panels (d), (e), and (f) are for non radial IMF

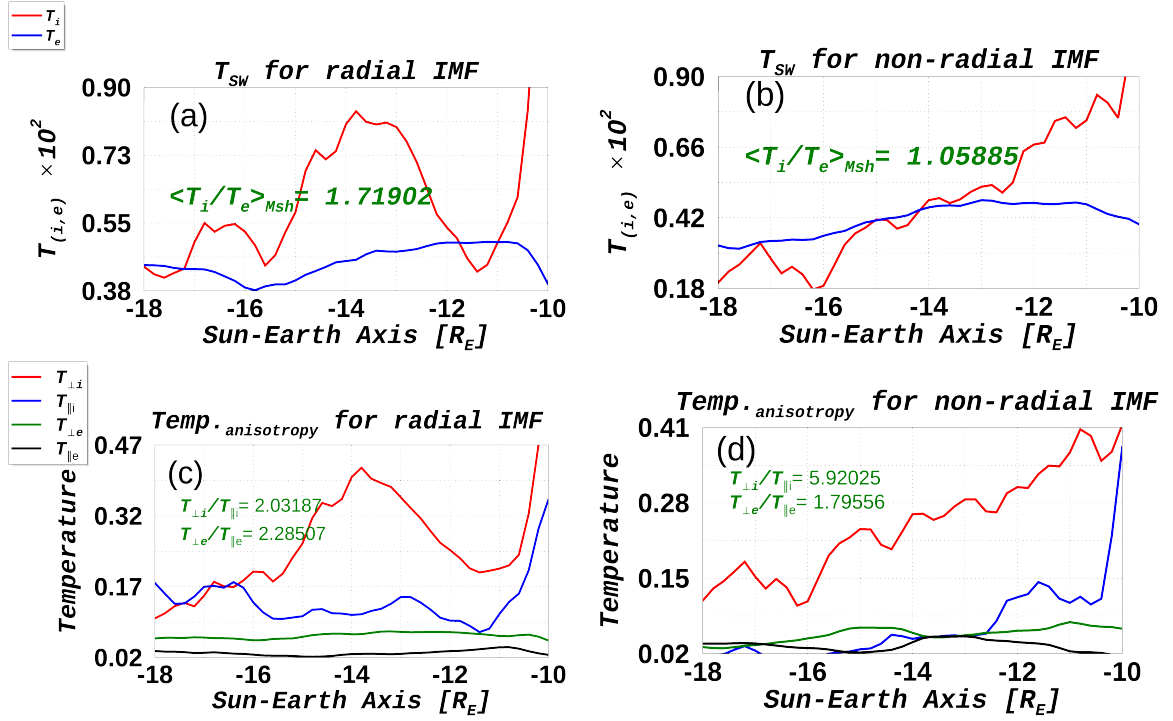


Figure 8. Ion and electron temperatures for both IMF orientations shown in panels (a), and (b). In panel (c) and ((d) temperature anisotropy for ions and electrons are shown. The T_i/T_e ratio is calculated in the magnetosheath in (a) and (b). The plots are taken from -18 to -10 R_E in the dayside magnetosphere.

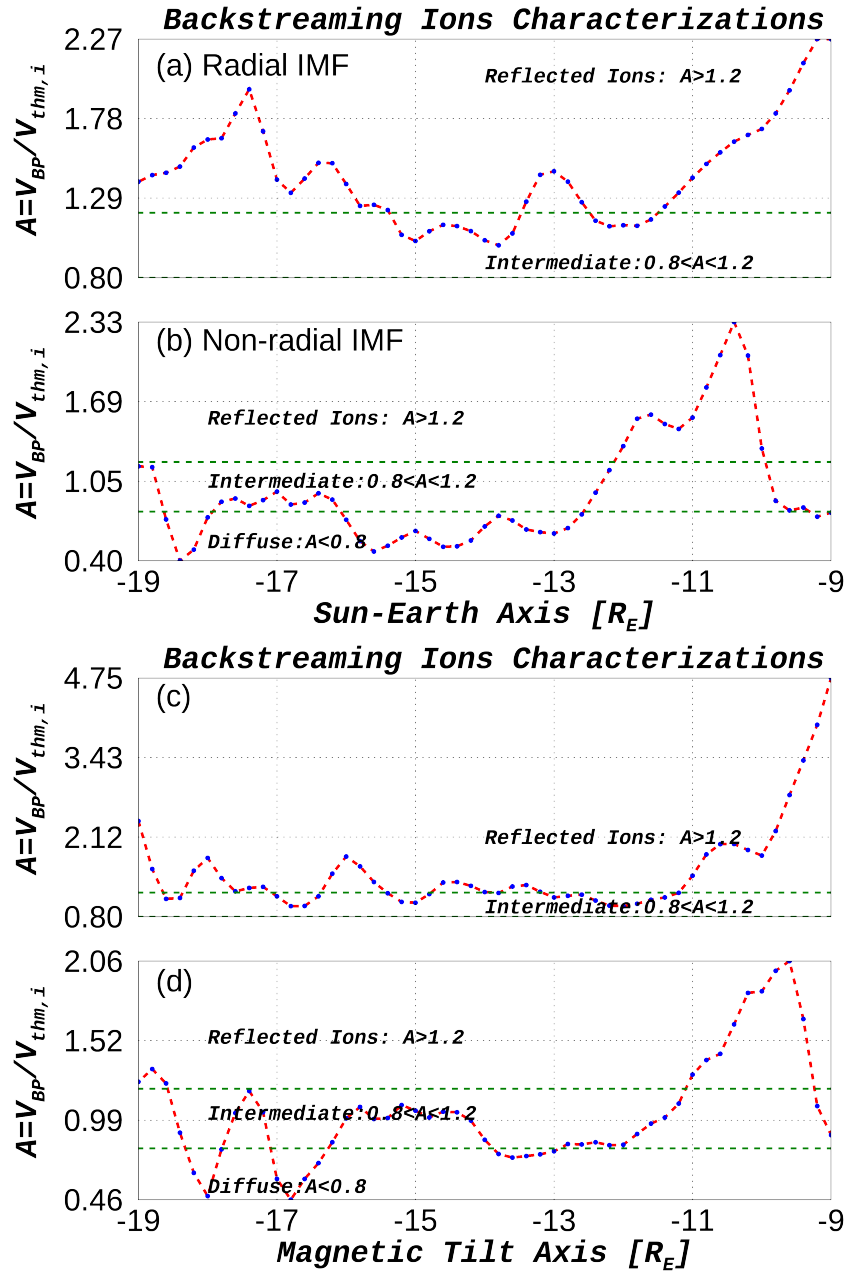


Figure 9. The characterization of backstreaming ions in the dayside magnetosphere based on their bulk flow ratio on thermal speed. Adopted from (Bonifazi & Moreno, 1981b). panel, a and b are taken along OX-axis in XZ plane and panels c, and d are taken along magnetic equator tilt for both IMF orientation. This figure shows the percentage of reflected and diffuse ions of the backstreaming ions.

Ion Velocity Distribution

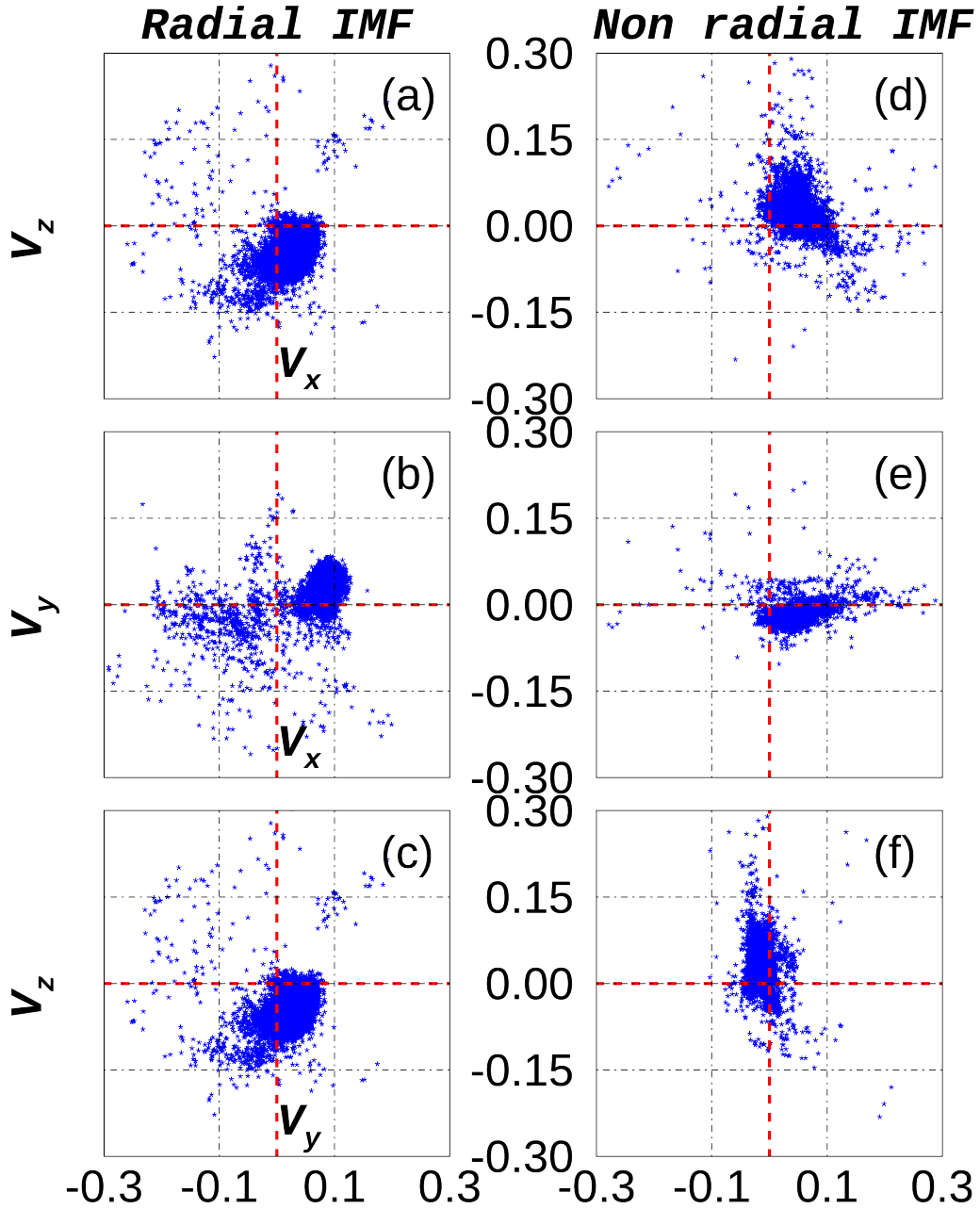


Figure 10. Ion Velocity distribution in the dayside measured from $-20R_E$ to the planet position ($z=y=0$) along Sun-Earth axis. Left panels are for radial IMF and right panels are for non radial IMF orientation.

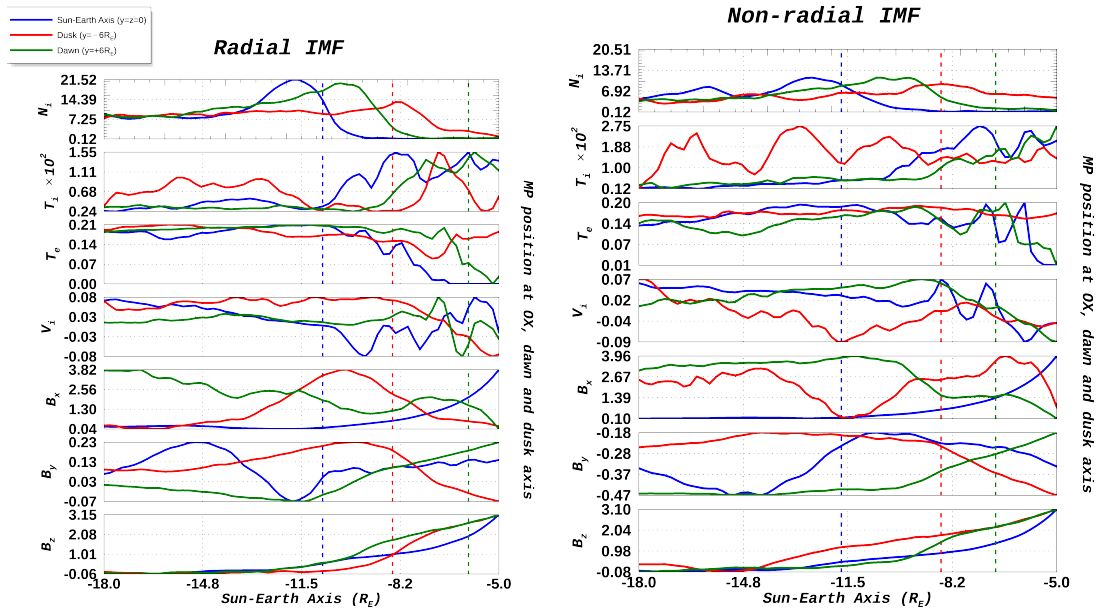


Figure 11. A set of plasma parameters, N_i , T_i , T_e , V_i , B_x , B_y , and B_z are plotted along XZ-plane at three different locations for both IMF orientations. These parameters are plotted along OX-axis and at ± 6 on both dusk and dawn directions. Vertical dashed lines show the MP position at the subsolar point (blue), dusk flank (red), and dawn flank (green) quantities show dusk-dawn asymmetry at the $\pm 6R_E$.